doi:10.26443/seismica.v3i2.1203

The influence of ground shaking on the distribution and size of coseismic landslides from the M_W 7.6 2005 Kashmir earthquake

Audrey M. Dunham *[1], **Eric Kiser** [1], **Jeffrey S. Kargel** [2], **Umesh K. Haritashya** [3], **C. Scott Watson** [4], **Dan H. Shugar** [5]

[1]Department of Geoscience, University of Arizona, Tucson, AZ, 85721, [2]Planetary Science Institute, Tucson AZ, 85719, [3]Department of Geology and Environmental Geosciences, University of Dayton, Dayton, OH 45469, [4]COMET, School of Earth and Environment, University of Leeds, Leeds, LS2 9JT, UK, [5]Water, Sediment, Hazards, and Earth-surface Dynamics (waterSHED) Lab, Department of Geoscience, University of Calgary, Canada

Author contributions: *Conceptualization*: A. Dunham, E. Kiser, J. Kargel, U. Haritashya. *Formal Analysis*: A. Dunham, E. Kiser. *Funding Acquisition*: E. Kiser, J. Kargel, U. Haritashya, C.S. Watson, D. Shugar. *Investigation*: A. Dunham, E. Kiser. *Methodology*: A. Dunham, E. Kiser. *Project Administration*: J. Kargel. *Supervision*: E. Kiser. *Validation*: A. Dunham. *Visualization*: A. Dunham. *Writing – original draft*: A. Dunham. *Writing – review & editing*: A. Dunham, E. Kiser, J. Kargel, U. Haritashya, C.S. Watson, D. Shugar.

Abstract Understanding the conditions that governed the distribution of coseismic landslide frequency and size from past earthquakes is imperative for quantifying the hazard potential of future events. However, it remains a challenge to evaluate the many factors controlling coseismic landsliding including ground shaking, topography, rock strength, and hydrology, among others, for any given earthquake, partly due to the lack of direct seismic observations in high mountain regions. To address the dearth of ground motion observations near triggered landslides, we develop simulated ground motions, including topographic amplification, to investigate these key factors that control the distribution of coseismic landslides from the M_w 7.6 2005 Kashmir earthquake. We show that the combination of strong peak ground motions, steep slopes, proximity to faults and rivers, and lithology control the overall spatial distribution of landslides. We also investigate the role of topographic amplification in triggering the largest landslide induced by this earthquake, the Hattian Bala landslide, finding that ground motion is amplified at the landslide initiation point due to the trapping of energy within the ridge kink as it changes orientation from E to NE. This focusing effect combined with predisposing conditions for hillslope failure may have influenced the location and size of this devastating landslide.

Production Editor:
Gareth Funning
Handling Editor:
Ake Fagereng
Copy & Layout Editor:
Hannah F. Mark

Received:
January 31, 2024
Accepted:
July 5, 2024
Published:
July 29, 2024

1 Introduction

Earthquake-triggered, or coseismic, landslides are the most destructive and fatal secondary geotechnical hazard related to earthquake shaking (Valagussa et al., 2019; Marano et al., 2009). To first order, it has been shown that earthquake magnitude and depth are important for the overall large-scale disturbance of the landscape (Marc et al., 2016; Tanyaş et al., 2018), but there are many other factors, such as the distribution of strong ground motions, topography, rock strength, and groundwater conditions that affect the distribution of coseismic landslides (Fan et al., 2018, 2019; Gorum et al., 2011). Of these factors, the distribution of strong ground motions is the most difficult to determine due to sparse seismic observations in these high mountain regions where coseismic landslides typically occur. Many studies compare landslide distributions to ground motion models based on attenuation relationships (e.g., USGS ShakeMap). While these can be reasonable first order estimations of peak ground motions in locations with observational data, they are much less well constrained in regions with little data and do not include how the wavefield interacts with topography, an important aspect of coseismic landslide initiation (Allstadt et al., 2018).

Another important controlling factor for coseismic landslide initiation is thought to be topographic amplification, or the interaction of the seismic wavefield with topography that causes scattering and diffraction at the free surface, leading to topographic effects that affect the intensity, frequency content, and duration of ground motions (Asimaki and Mohammadi, 2018; Assimaki and Jeong, 2013; Dunham et al., 2022; Lee et al., 2009; Hartzell et al., 2016). Typically, ridges focus seismic waves, causing amplification through constructive interference, whereas valleys cause seismic waves to scatter, decreasing seismic wave amplitudes (deamplification). Coseismic landslides have been shown to initiate higher on hillslopes than rainfall-induced landslides, likely due to the increase in seismic wave amplitudes at ridge tops (Meunier et al., 2007; Rault et al., 2019, 2020). Topographic amplification, along with the overall frequency content of the earthquake, also impacts landslide size. Lower frequencies generate amplifications with larger depths and lateral extents,

*Corresponding author: adunham@usgs.gov. Now at US Geological Survey, Seattle Field Office, Seattle WA, 98195.

allowing the failure of deeper and larger landslides compared to higher frequencies (Bourdeau et al., 2004; Kramer, 1996). Using numerical modeling of ground motions and topographic amplification, Dunham et al. (2022) showed that low-frequency topographic amplification, along with steep slopes and high elevations, contributed to the initiation of the largest landslides from the 2015 M_w 7.8 Gorkha, Nepal earthquake. Although topographic amplification is thought to have a major impact on coseismic landslide distributions, the study of this phenomenon is again stifled by the lack of observational data in high mountain regions where coseismic landslides are typically occurring.

The 2005 M_w 7.6 Kashmir earthquake (Fig. 1) was the most devastating earthquake in Pakistan's history, causing 87,000 fatalities (Mahmood et al., 2015), which include deaths from the 2000-3000 coseismic landslides both directly as well as indirectly from blocked roads and communication loss (Kamp et al., 2008). The largest and most devastating landslide, the Hattian Bala landslide, caused ~1000 deaths and destroyed a village (Dunning et al., 2007; Harp and Crone, 2006) (Fig. 1, black box). While extensive documented landsliding from this earthquake provides an excellent case study for quantifying the impacts of ground shaking on coseismic landslide distributions in high mountain regions, there is a lack of observational seismic data from this event. There are no available seismic stations within ~100 km of the fault and the only model of peak ground motions provided by the USGS ShakeMap is fairly unconstrained because it is generated using only felt intensity data and empirical attenuation relationships, rather than peak amplitude data from seismic stations. This limits our ability to connect peak ground motions and topographic effects to landslide initiation, information which is particularly important for improving real-time coseismic landslide prediction models for future hazard mitigation (Allstadt et al., 2018).

To address this limitation and determine the dominant factors controlling co-seismic landslide initiation, we use numerical modeling of the seismic wavefield to calculate peak ground motions and topographic amplification values for the landslide-affected region of the 2005 Kashmir earthquake. Although many studies have investigated the landslide distribution from this earthquake, few have explored the relationship between ground shaking and landslides, likely due to the lack of observational data. One such study by Khan et al. (2020) modeled ground shaking from this earthquake to compare to the damage and coseismic landslide distribution, but they used a point source characterization of the earthquake, limiting their ability to accurately model the shaking without including the complexities of the rupture. We model the wavefield from the 2005 Kashmir earthquake using a kinematic source description in a domain with a topographically complex free surface to quantify the role that topography plays in amplifying the wavefield and initiating landslides. To gain a holistic view of the landslide distribution, we also compare it to other important geomorphic and geologic factors that impact initiation. By using ground motion simulations compared to traditional methods, we can better understand the relationship between ground shaking, topographic amplification, and coseismic landslide initiation, therefore offering crucial insights into past and future coseismic landslide distributions, including implications for the largest triggered landslides.

2 Kashmir earthquake characteristics and tectonic setting

The Kashmir earthquake occurred on October 8, 2005 at the western termination of the Indian-Eurasian collision zone, ~18 km N-NE of the city of Muzaffarabad (Basharat et al., 2021; Kaneda et al., 2008) (Fig. 1). The earthquake ruptured for ~25 s both bilaterally and updip along the Muzaffarabad thrust fault with a ~2 km/s average rupture velocity and peak slip of ~7 m near the city of Muzaffarabad (Avouac et al., 2006; Parsons et al., 2006; Pathier et al., 2006; Yan et al., 2013). The Muzaffarabad fault dips ~30° NE and is located along the western limb of the Hazara-Kashmir Syntaxis (HKS), a major antiformal structure that is bounded by the Murree Thrust, a NW dipping fault that locally defines the Main Boundary Thrust (MBT) (Dunning et al., 2007). The earthquake produced a ~70 km-long surface rupture, the first modern earthquake in the Himalaya to produce a documented surface rupture (Avouac et al., 2006; Kaneda et al., 2008), and was the most devastating earthquake in Pakistan's history, killing 87,000, injuring 69,000, and leaving 2.8 million homeless (Mahmood et al., 2015; Peiris et al., 2006; Petley et al., 2006). A previous major earthquake (M>8) in this region was just to the south in 1555 (Fig. 1, inset), but based on damage reports from this event, it is likely that it ruptured on a different fault than the 2005 earthquake (Kaneda et al., 2008).

Most of the rocks here are highly faulted and fractured sedimentary/metasedimentary rocks due to the multitude of faults and folds in the region (Shafique et al., 2016). The Miocene Murree Formation (Fm) makes up most of the study area (Fig. 1) and is primarily mudstone, siltstone, and sandstone, with variable deformation throughout the extensive area, from undeformed to highly cleaved and fractured (Kamp et al., 2008). The highly fractured and cleaved Precambrian slate, phyllite, shale, and limestone of the Hazara Fm (southwestern) and metamorphic rocks of the Salkhala Fm (northeastern) also make up much of the region (Kamp et al., 2008). The Muzaffarabad Fm is particularly important for landslide susceptibility and is composed of highly fractured dolomites and limestones (Kamp et al., 2008). Other formations include a variety of granite, sandstone, siltstone, mudstone, conglomerate, schist, limestone, and dolomite; we refer to Kamp et al. (2008) for the full descriptions of the other units. The many fault zones surrounding the HKS consist of very weak and deformed rocks, making this region particularly primed for landsliding during an earthquake (Massey et al., 2018).

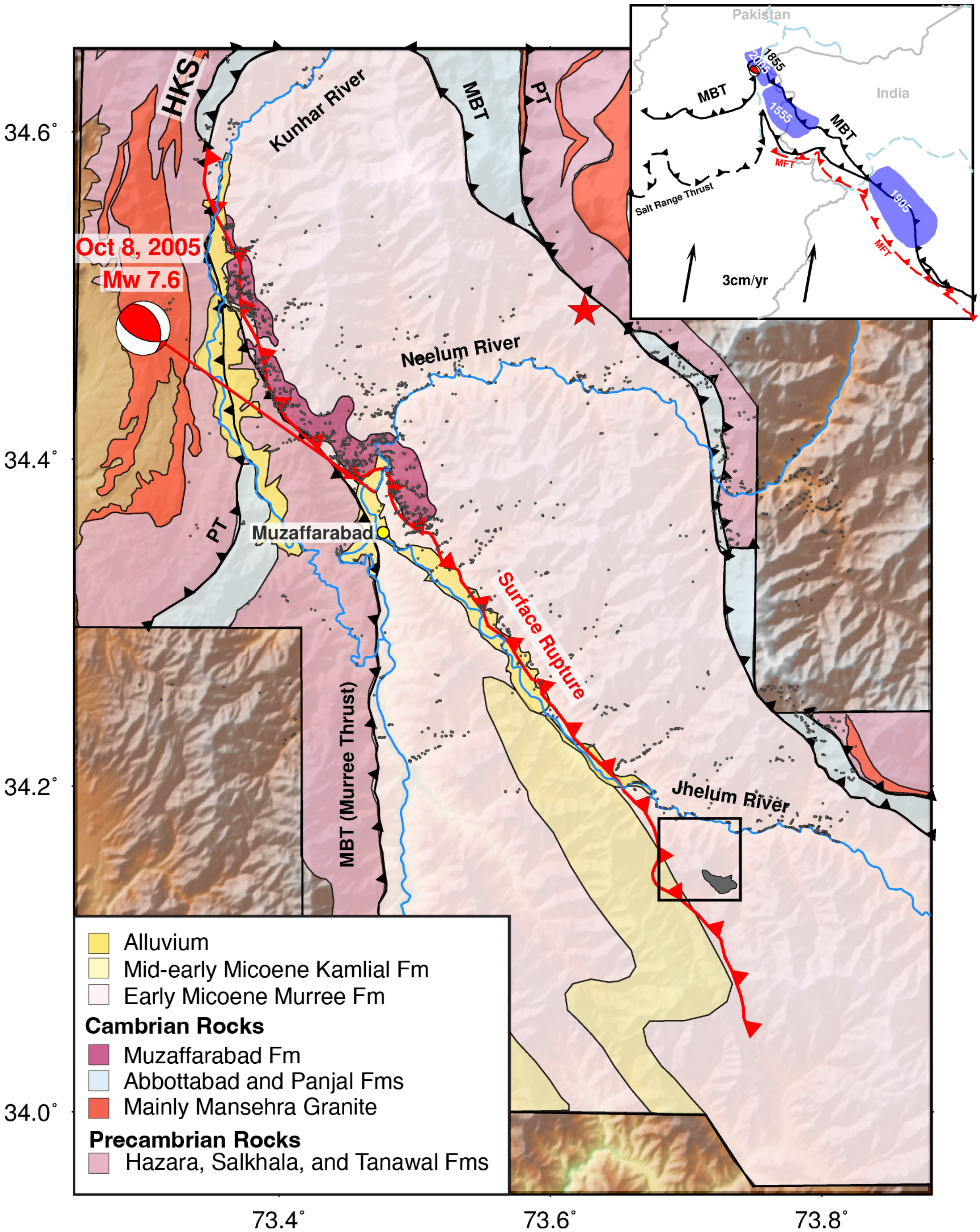

Figure 1 Map of the tectonic setting of the M_W 7.6 2005 Kashmir Earthquake, red focal mechanism shown at the location of the earthquake centroid and epicenter shown as a red star. Geologic map in the background is modified from Kaneda et al. (2008) and Basharat et al. (2021). Thick black lines are regional faults with triangles pointing to the upthrown block, red line is the surface rupture. MBT- Main Boundary Thrust (also Murree Thrust), PT – Panjal Thrust, HKS – Hazara-Kashmir Syntaxis. Blue lines are major rivers. Gray dots are landslides from Sato et al. (2007) and the Hattian Bala landslide polygon (gray field) plotted in the black square is from Basharat et al. (2016). Inset shows this region in a tectonic context, including major thrust faults in the region such as the MBT, Salt Range Thrust, and MFT – Main Frontal Thrust, and arrows indicating the direction of convergence at a rate of 3 cm/yr. Blue polygons are the rupture areas of paleoseismic events: 1555 – 7.6-8, 1905 – M7.8-7.9, 1885 – M7.1-7.5 same rupture area as 2005 event, shown as a red focal mechanism, magnitudes of paleoseismic event magnitudes from Bilham (2019).

3 Kashmir earthquake landslides

3.1 Coseismic landslides

Over 60 articles have been published on the landslides caused by the 2005 Kashmir earthquake at various resolutions and spatial coverages (Basharat et al., 2021). These studies use a variety of different mapping methods, such as satellite imagery, repeat photography, field investigation and validation, and a combination of these methods (Basharat et al., 2014, 2016; Dunning et al., 2007; Harp and Crone, 2006; Kamp et al., 2008; Khattak et al., 2010; Mahmood et al., 2015; Owen et al., 2008; Saba et al., 2010; Kamp et al., 2009; Khan et al., 2013; Sato et al., 2007). Studies that mapped the whole affected region (Basharat et al., 2014, 2016; Kamp et al., 2008; Owen et al., 2008; Sato et al., 2007) mapped between 2000-3000 landslides, mostly shallow rock falls and slides (Harp and Crone, 2006; Kamp et al., 2008; Sato et al., 2007). Collectively, these studies have found landslides primarily occurred on the hanging wall of the Muzaffarabad fault, coincident with the strongest ground shaking (Sato et al., 2007). Most landslides occurred close to rivers and active faults (<1km Sato et al., 2007) as well as within the Murree Fm, which makes up >50% of the region (Fig. 1) (Kamp et al., 2008). However, the highest landslide area density occurred within the Muzaffarabad Fm (Kamp et al., 2008), located on the hanging wall along the surface rupture (Fig. 1). Most landslides are at elevations between 1000-1500m, at slopes 25-35° and on S-SW facing slopes (Kamp et al., 2008). Extensive fissuring, particularly in the Muzaffarabad Fm, was documented and thought to cause increased susceptibility for future landslides (Owen et al., 2008). Landslides caused ~1000 direct and many indirect casualties due to communication loss (Kamp et al., 2008).

For this study, we use the database from Sato et al. (2007), who mapped 2424 landslides over most landslide-affected regions using 2.5 m resolution SPOT-5 imagery. We chose this database because it uses pre- and post-earthquake satellite imagery for mapping, comparatively high-resolution imagery, and maps the whole landslide-affected area, except for some snow-covered regions at high elevations. While the authors acknowledge the potential for some pre-earthquake landslides in their database due to the timing of the imagery, other databases only used post-earthquake imagery (Basharat et al., 2014, 2016; Kamp et al., 2008).

3.2 Hattian Bala landslide

The largest landslide from the 2005 Kashmir earthquake was the Hattian Bala landslide (~80-85 x 10^6 m^3), which buried the village of Dandbeh, killing ~1000 people according to local reports (Dunning et al., 2007; Harp and Crone, 2006) (Fig. 1, black box). This event occurred in the Murree Fm and was located at a cluster of small pre-earthquake landslides (Kamp et al., 2008). From investigating 1992-2001 satellite imagery, Dunning et al. (2007) found that this region was deforming before the rock avalanche and that the earthquake shaking caused the rock mass to exceed a critical failure threshold (Dunning et al., 2007). The landslide dammed a tributary of the Jhelum River (Karli River), creating two lakes that were a major concern for downstream villages, namely Hattian (Harp and Crone, 2006). These dams were partially breached in February 2010, directly damaging 24 homes and causing a landslide from reservoir drawdown, which destroyed an additional 174 structures and forced the evacuation of ~1000 residents (Konagai and Sattar, 2011). Since the dam failure in 2010, the landslide mass has not experienced significant changes and likely does not pose an imminent hazard to the region (Sattar and Konagai, 2023). This primary Hattian Bala rock avalanche occurred 32 km SE of Muzaffarabad, far from the region of densest landsliding and it has been speculated that topographic amplification of the seismic waves was an important factor in triggering this event (Basharat et al., 2021; Dunning et al., 2007; Harp and Crone, 2006). In this study, we use simulated ground motions at this location to investigate topographic amplification as a possible additional triggering mechanism for the Hattian Bala landslide. Because it was shown that there was a high probability of slope failure prior to the earthquake, our calculations of topographic amplification cannot show a causal effect; rather, this work investigates whether the characteristics of topographic amplification at this particular location are consistent with the hypothesis that the occurrence of this large landslide was influenced by the interactions of the seismic wavefield with topography.

4 Data and methods

4.1 Numerical modeling

4.1.1 Source models

To simulate the ground shaking from the 2005 Kashmir earthquake, we represent the seismic source as a kinematic rupture, which we define using a finite fault model from the earthquake. Finite fault models allow for the simulation of ground motions up to ~1 Hz by matching the source inversion to both teleseismic and geodetic data but are more limited for higher frequency simulations. The source model used in this study was generated by jointly inverting teleseismic waveforms in the 0.01-1 Hz frequency band and surface slip measurements from the sub-pixel correlation of ASTER imagery (Avouac et al., 2006) (Fig. 2). Each slip patch is defined by five triangular source time functions that are separated in time by 50% of the rise time of the subfault (Supplementary Fig. S1). This method is used because it requires less regularization and linearizes the inversion (Chen et al., 2018). The rise times of the Avouac et al. (2006) kinematic source model are homogeneous across the fault with a constant value of 3 s (Fig. 2b). In the near-field, we expect ground motions to have energy at frequencies >1 Hz that are not exhibited by the finite fault model. To generate ground motions that have energy above 1 Hz, we develop a second source by modifying the Avouac et al. (2006) model to include heterogeneous and shorter rise times that vary with the magnitude of slip and depth of the subfaults (Graves and Pitarka) (Fig. 2c). This method allows us to keep the slip distribution and rupture velocity the same as the original finite fault model, which is well constrained by the teleseismic and geodetic observations, while increasing the frequency content of the source in a way that has been observed in other crustal earthquakes, though we acknowledge that the modified rise times do not necessarily represent the true source properties.

Rise times typically increase in shallow depth and high slip patches on the subfault, with longer rise times related to lower frequency seismic waves. We calculate rise times (T_i) using:

$$T_i = \begin{cases} 2ks_i^{\frac{1}{2}}; d < 5km \\ ks_i^{\frac{1}{2}}; d > 8km \end{cases} \tag{1}$$

where s_i is the slip on the individual subfault and k is a constant derived from fault's average rise time. Typically, the average rise time is calculated based on the moment release on the fault, but here we calculate k based on the relationship between the highest slip and a rise time of 3 s from the original source. Because rise times are based on slip and some slip patches have very low or 0 m slip, we define a minimum rise time of 0.7s, twice the minimum period resolved by our mesh. For both sources, we decrease the subfault size from 4 x 3.5 km to 250 x 250 m spacing to appropriately sample the source at the same interval as the mesh. We only allow sources at depths greater than 1 km, reducing numerical inconsistencies at the free surface while retaining the majority of the moment of the earthquake. We will refer to the original low frequency source as ORIG and the modified higher frequency source as HF.

4.1.2 Meshing and synthetic waveform generation

We simulate ground motions from the kinematic rupture from the Kashmir earthquake in a structured hexahedral mesh with high resolution topography using the Spectral Element Method (SEM). The SEM is the most appropriate method to simulate the wavefield because it naturally incorporates high resolution topography at the free surface so that we can investigate the effects of topography on the wavefield and on landslide initiation. The SEM was developed 40 years ago in computational fluid dynamics (Patera, 1984) and is now used to model 2-3D seismic wave propagation. It solves the weak formulation of the equations of motion and uses high-order Lagrange polynomials to discretize over each element based on the Gauss-Lobatto-Legendre (GLL) integration rule (Komatitsch and Tromp, 1999). The SEM is implemented in the SPECFEM3D software package (Komatitsch and Tromp, 2002a,b) to generate 3D wavefield simulations for both ORIG and HF earthquake sources. We first generate a numerically stable mesh with 250 m resolution topography that encompasses both the kinematic rupture and the coseismic landslide distribution. The mesh is 71 km x 78 km x 18 km in depth, with 250 m elements in the upper 1 km buffer layer, doubling at 1 km depth to increase the element size to 500 m for the remainder of the model (Fig. 3). The bottom of the buffering layer is the 250 m resolution topography that has been smoothed using a moving average with a radius of 2 km, which aids in decreasing the distortion of free surface elements. The mesh has ~1.2 million elements and is numerically resolved up to 2.7 Hz and will be referred to as the topography mesh.

Because of a lack of high-resolution 3D velocity models in this region, we use a 1D regional velocity model (Mahesh et al., 2013) modified with a 1 km thick slow velocity layer at the surface with a linear Vs gradient between 1500 and 3200 m/s (Table 1). Vs = 1500 m/s is the transition between site class B (rock, Vs < 1500 m/s) and site class A (hard rock, Vs > 1500 m/s) according to the NERHP soil site classifications (Dobry et al., 2000), making it a reasonable estimate for our surficial slow velocity layer in this high mountain region. Our limited knowledge of subsurface velocities hinders our ability to accurately model ground motions (Lee et al., 2007). Previous studies have shown that the amplitudes of seismic waves are impacted by the interplay between near surface velocity variation and topography (Assimaki and Jeong, 2013; Dafni and Wartman, 2021; Hailemikael et al., 2016; Hartzell et al., 2013; Hailemikael et al., 2016). This 1D velocity model as well as others for the region (Mir et al., 2017) show minimum Vs values at the surface between 2-3.5 km/s but are insensitive to the structure of the upper few kilometers of the crust. By adding a slow velocity layer to the upper 1 km of the crust, we are approximating a known decrease in velocity near the free surface that is not defined by these coarser models. Finally, it should be noted that the models do not include intrinsic attenuation which has little effect on the seismic wavefield results at these local distances and relatively low frequencies.

Depth (km)	Vp (km/s)	Vs (km/s)
0	2.8	1.5
0.25	3.475	1.925
0.5	4.150	2.350
0.75	4.825	2.775
1	5.5	3.2
4	5.85	3.4
18	6	3.5

Table 1 Table showing the seismic wave speeds defined within the mesh by depth. The top 1 km is a linear gradient from Vs = 1.5 km/s to the top of the 1D velocity model from Mahesh et al. (2013).

Horizontal peak ground velocity (PGV) is calculated at every element at the surface during the wavefield simulations by taking the peak velocity value between the NS and EW components. There is debate in the literature about the best ground motion metric for understanding coseismic landslide initiation, including peak intensities (peak ground acceleration (PGA) and PGV), duration, and cumulative metrics such as Arias Intensity (Jibson et al., 2000; Jibson and Tanyaş, 2020; Nowicki Jessee et al., 2018). We have chosen to use PGV as our ground shaking metric due to the relatively low

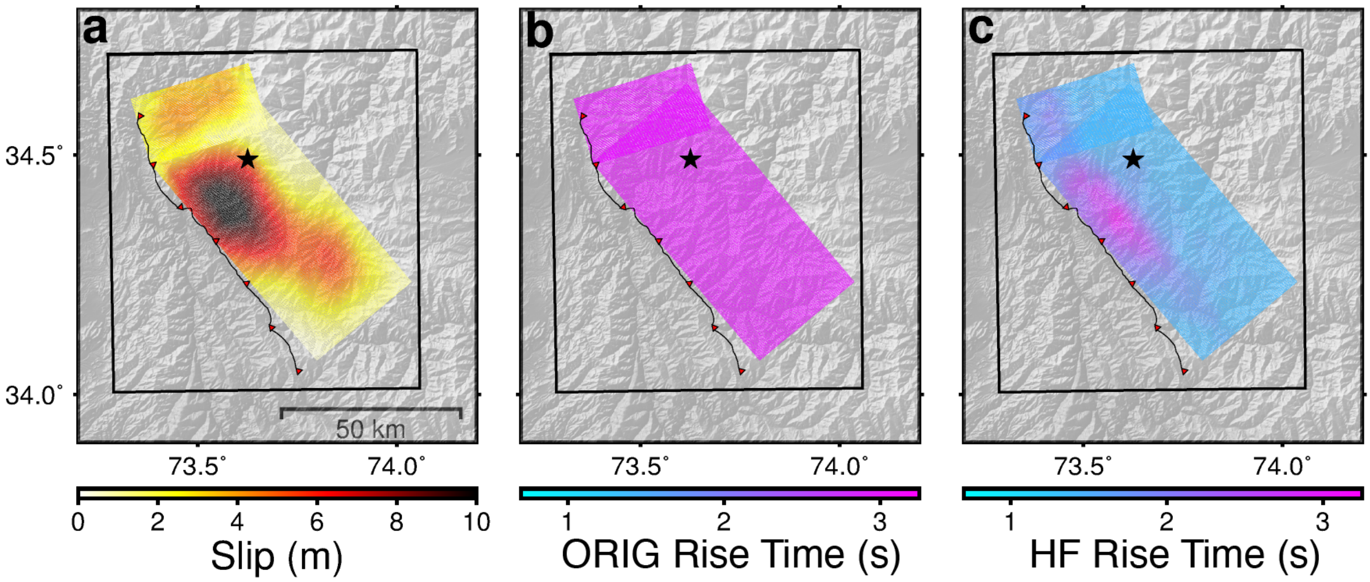

Figure 2 **(a)** Slip model from Avouac et al. (2006). Slip for each subfault is the sum of all 5 source time functions. **(b)** Homogeneous rise time distribution from Avouac et al. (2006), used in source ORIG. **(c)** Modified rise time distribution used in source HF. Rise time is shown as the average for each subfault from the 5 source time functions, see Supplementary Fig. S1 for the distribution of slip and rise times for all 5 source time functions. Surface rupture is shown as the black line with red triangles, epicenter is the black star, and black square denotes the meshed region.

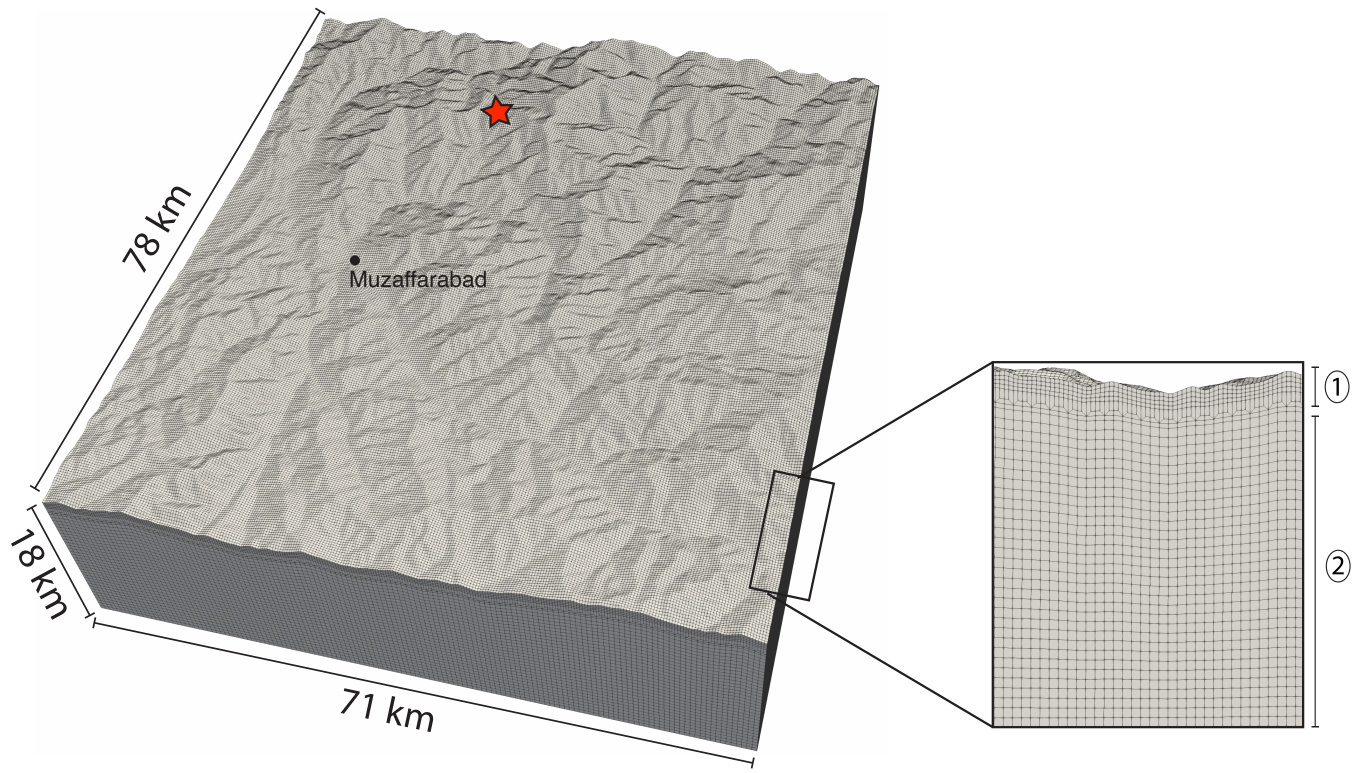

Figure 3 Numerical mesh with 250 m topographic resolution, dimensions are shown on the edges of the mesh. The city of Muzaffarabad (black circle) and epicenter (red star) are shown for reference. Inset shows a zoom-in of the mesh. (1) is a 1 km thick layer with 250 m elements with a doubling layer at the base of this layer, (2) is a 17 km thick layer with 500 m elements. Black square in Fig. 2 shows the outline of the meshed region in map view.

frequency content of these simulations and because it has been shown to have significant control on landslide initiation and size (Dunham et al., 2022; Massey et al., 2018; Nowicki Jessee et al., 2018). We verify these ground motions against the USGS ShakeMap due to the lack of seismic or high-rate geodetic stations in the region during the earthquake. While this model is fairly unconstrained, it is the only available model that incorporates real data from the earthquake into the ground motion result, making it our best means of comparison. This shows that our simulations using the HF source and 1D layered velocity model with a slow velocity layer have the best fits to the ShakeMap, while simulations using a homogeneous velocity model from IASPI91 (Vp = 5.8 km/s, Vs = 3.36 km/s, 2.7 kg/m^3) (Kennett and Engdahl, 1991) (Supplementary Fig. S2) have much lower PGVs compared to the ShakeMap. Therefore, we present the results and discussion in the main-text using the 1D layered model and show results from simulations with a homogeneous velocity in the Supplement for both ORIG and HF (Supplementary Text S1 and Supplementary Fig. S3). Because there is not an available 3D velocity model that incorporates detailed shallow velocity structure (mapped Vs30), we are likely under-representing seismic amplitudes and frequency content, and therefore these results should not be used for primary seismic hazard applications.

Generally, topographic amplification of the seismic wavefield is calculated by comparing the ground shaking values in a topographically complex mesh to ground shaking values in a flat mesh. The choice of elevation of the flat mesh is critical to the calculation of amplification, as seismic amplitudes are not only affected by topography but also attenuation due to geometrical spreading. Supplementary Fig. S4 shows how flat meshes with different elevations change amplification values. To decrease the effects of geometrical spreading in our amplification result, we calculate PGV for ORIG and HF in a suite of flat meshes with free surface elevations that span the elevation range of our topography mesh. We then conduct a 1D interpolation of these values to the elevation of our topography mesh at each point on the surface to match the expected distance traveled by the wavefield for both the flat and topography ground motions, generating elevation corrected flat PGVs. Because this is a surface rupturing earthquake, our sources reach close to the free surface, so we decrease the interval between the flat meshes to 500 m at the lower elevations. Our flat mesh elevations are 500, 1000, 1500, 2000, 3500, and 5000 m. The flat meshes all have a doubling layer at 1 km depth so that they have the same resolvable frequency content as the topography mesh. The flat meshes also have the same elastic properties as the topography mesh. To calculate a value of topographic amplification, we take the percent difference between the maximum horizontal PGV of the elevation corrected flat mesh and the topography mesh:

$$Amplification\% = \frac{PGV_t - PGV_{fc}}{PGV_{fc}} \times 10 \qquad (2)$$

Where PGV_t is horizontal PGV within the topography mesh and PGV_{fc} is the elevation corrected horizontal PGV derived from flat mesh simulations.

4.2 Landslide catalog processing

To investigate the possible causes of landslide initiation from the 2005 Kashmir earthquake, we determine topographic, lithologic, hillslope position, and seismic parameters (i.e. PGV and topographic amplification) at each landslide location from the Sato et al. (2007) catalog. The maximum values within landslide polygons of ground shaking parameters (horizontal PGV and horizontal PGV amplification) from our numerical simulations (both ORIG and HF) and topographic parameters (slope and elevation) from SRTM 30 m DEM (Farr et al., 2007) are used for the analysis. We also calculate local relief by taking the difference between the maximum and minimum elevation of the 30 m DEM within a moving window with a radius of 1 km, taking the maximum value within each landslide polygon. The landslides in this database are not subdivided into source and runout, so we calculate these parameters for the whole landslide-defined area. We determine the lithology of each landslide using the geologic map from Kaneda et al. (2008) that was modified from Calkins et al. (1975). The geologic unit assigned to each landslide is determined by which unit covers the highest percent of the landslide area. We also calculate the landslide location along the hillslope (D_{st}, normalized river distance Rault et al., 2019) to determine if coseismic landslides are preferentially located along ridges or within valleys and frequency-area distribution (FAD) curves for a subset of landslide parameters to demonstrate their control on landslide size. These methods are expanded upon in Supplementary Texts S2 and S3 and Fig. S5. While rainfall and soil saturation prior to an earthquake are important factors controlling overall coseismic landslide distributions, we do not include this in our analysis because of the dry conditions documented before this event (Petley et al., 2006).

5 Results

5.1 Wavefield snapshots

Snapshots of the seismic wavefield demonstrate wave propagation through time as the rupture starts at the hypocenter (black star, Fig. 4 and Supplementary Movies S1 and S3) and propagates updip and bilaterally along the fault. Vertical ground motions at the surface are clear ~3 s after rupture initiation, where a large, low frequency positive (up) wavefront can be observed propagating SW and then W-NW. This low frequency pulse is due to the large amplitude of slip at the central zone of the rupture. The breaking of this asperity (between 8-10 s) is coincident with the rupture reaching the surface (Fig. 4, line with red triangles), causing a clear decrease in amplitude as the large, low amplitude wave crosses the surface trace and a step in the once continuous wavefront. Larger amplitude, south propagating waves are then observed emanating along the fault trace. Both sources demonstrate similar wavefield properties, although HF has a higher frequency component due to the modification of source rise times. The hanging wall effect, or the increase in ground motion amplitudes on the hanging wall (Abra-

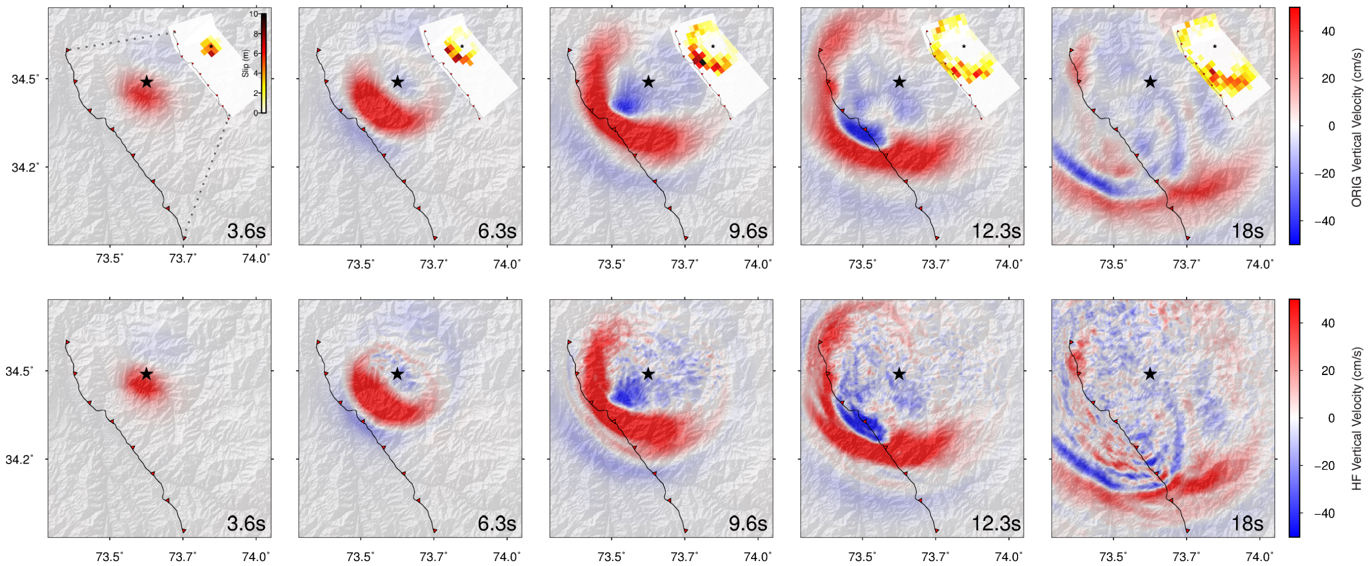

Figure 4 Snapshots of the vertical velocity wavefield for ORIG **(top)** and HF **(bottom)**. Black star is the hypocenter, line with red triangles denotes the surface rupture, and timestamps are shown in the lower right corner for each snapshot. Inset shows the slip on the fault at each time step as the sum of slip between each snapshot.

hamson and Somerville, 1996; Oglesby et al., 1998), is also clear for both sources as amplitude significantly decreases southwest of the surface rupture. Because we do not prescribe a fault surface as a discontinuity in our numerical mesh, this effect is due to the proximity of the free surface to the rupture rather than the trapping of energy between the fault and the free surface. HF has higher amplitudes on the footwall than ORIG, likely due to subfault sources with shorter rise times that rupture near the fault trace with small slip values. Supplementary Fig. S6 shows snapshots of the peak horizontal motion, also shown as movies in Supplementary Movies S2 and S4, which clearly show the interactions of the wavefield with topography, where ridges are amplified at different points throughout the rupture. Both snapshot components clearly show how the frequency content of the two sources varies, with the major low frequency components being the same for ORIG and HF, but the wavefield from HF exhibiting much shorter wavelength features within these broader wavefronts. They also demonstrate how the directivity of the rupture focuses the strongest shaking at the surface rupture as it initially travels SW and then NW and SE as it travels along the surface rupture.

5.2 Peak ground motions

Figs 5a and 5c shows the horizontal PGV for ORIG and HF, respectively. Fig. 5e also shows a selection of waveforms for ORIG (blue) and HF (black), denoting the values of PGV for each waveform in the upper right corner. The highest values of PGV for both sources are concentrated at the surface rupture on the hanging wall, an expected result given the location of the primary asperity in the slip model. This slip and ground shaking concentration is a common phenomenon for surface rupturing earthquakes (Kagawa et al., 2004). As we saw in the wavefield snapshots (Fig. 4, Supplementary Fig. S6), the hanging wall effect is also clear for PGV, with amplitudes decreasing significantly southwest of the fault trace. HF has higher amplitude PGVs away from the fault because of the smaller rise times prescribed to the low slip values, allowing for higher energy radiation in HF at the down dip edge of the fault than ORIG. We also see larger amplitudes across the fault to the southwest for HF, which we observed in the wavefield snapshots. Fig. 6a shows the difference between PGVs of ORIG and HF, showing that variation between PGV is concentrated away from the highest slip amplitude, where we have changes in PGV based on variations in rise time. Overall, these differences are quite small, confirming that the amplitude of ground shaking between the two sources is not changing significantly at a large scale but is mainly concentrated on smaller scale features.

5.3 Topographic amplification

Figs 5b and 5d show topographic amplification values for ORIG and HF, respectively. Positive topographic amplification is mostly concentrated at ridges, and negative amplification in valleys, as expected from previous studies (e.g. Dunham et al., 2022; Harp et al., 2014; Hartzell et al., 2016). Amplification ranges between -60% and 100%. The orientation of ridges with respect to the initial high amplitude wavefront controls the pattern and extent of topographic amplification. Ridges trending in the direction of propagation tend to be amplified along the ridge top, whereas smaller auxiliary ridges trending perpendicular to the direction of propagation tend to have amplification on the ridge side facing in the direction of propagation. This phenomenon, where amplification tends to be more prominent on the slopes of ridges facing away from the incident wavefield when this wavefield deviates from the vertical propagation path, is seen in other modeling and observational studies (Dunham et al., 2022; Meunier et al., 2008; Khan et al., 2020; Maufroy et al., 2014). This is particularly

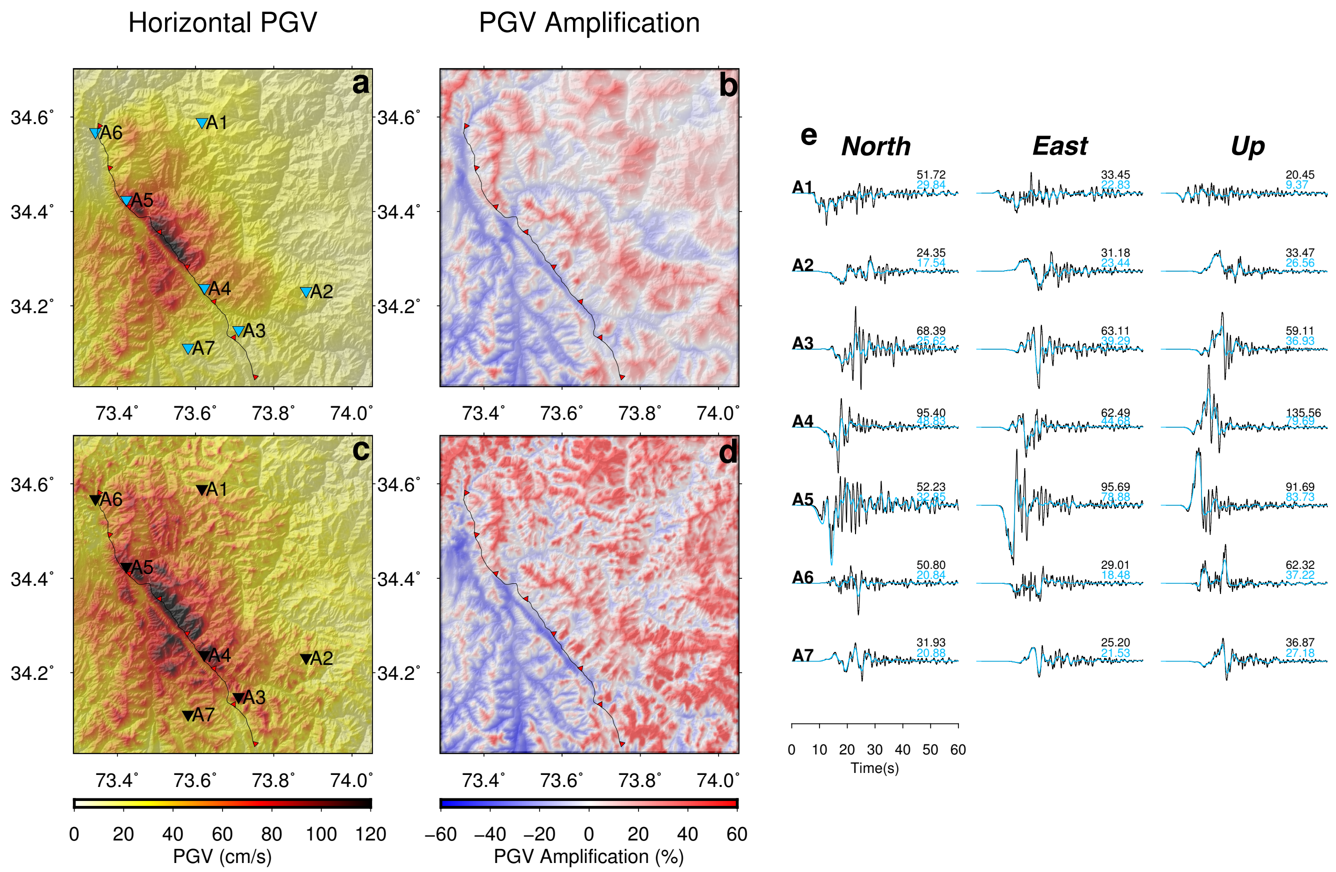

Figure 5 **(a)** Horizontal PGV and **(b)** topographic amplification for ORIG. **(c)** Horizontal PGV and **(d)** topographic amplification for HF. Line denotes surface rupture. **(e)** Example waveforms for the north, east, and vertical component of 7 stations (plotted on a/c) for ORIG (blue triangles) and HF (black triangles). PGV of each seismogram labeled in cm/s (ORIG – blue, HF – black).

evident at ridges just east of the surface rupture, where ridges trending NE are amplified on their SE facing side due to the SE propagation of the rupture near the surface rupture.

HF shows much more high frequency amplification, meaning that smaller ridges are amplified compared to ORIG, which is also exemplified in the waveforms (Fig. 5e), showing much higher frequency content for HF than ORIG. This is clear from the differences plotted in Fig. 6b, where the largest differences between amplifications are on small-scale features, with little variation for larger scale ridges. From the snapshots of the wavefield, we can see much shorter wavelength phases for HF compared to ORIG, contributing to the fact that the wavefield within shorter wavelength (smaller) ridges is being amplified. Amplification values are also larger on average for HF compared to ORIG, demonstrating that higher frequencies not only increase the number of ridges being amplified but also increase the absolute value of amplification. A notable feature with significantly increased amplification from HF compared to ORIG is the causative ridge of the Hattian Bala landslide, outlined in Fig. 6.

Although we have increased the frequency content of our simulations between ORIG and HF, this is only up to ~ 2.7 Hz. Topographic amplification is highly dependent on frequency content, with higher frequencies causing the amplification of shorter wavelength topographic features. Along with the relatively coarse resolution of the free surface topography of our numerical mesh, we are likely not accurately representing the topographic amplification of small ridge features. We are, however, representing the regional amplification patterns well, as seen by the increase in the number of smaller scale amplified features from ORIG to HF, but little variation in the overall amplification pattern (Figs 5b, 5d, 6). Therefore, even though our result is frequency limited (< 2.7 Hz), we can use topographic amplification to comment on regional patterns as well as large-scale topographic features.

5.4 Predictive capability of landslide parameters

Following the methods of Chung and Fabbri (2003) and Harp et al. (2014), we determine the predictive power of landslide parameters using a “ratio of effectiveness”. The ratio of effectiveness (R_{eff}) is defined by R_v/R_{tot}, where R_v is the percent of landslide area within a range of a parameter compared to the total area of that parameter class in the study region (defined by the mapping area of Sato et al., 2007) and R_{tot} is the percent of landslide area within the whole study region. In other words, R_{eff} shows how important a parameter is for landslide generation by comparing the percent of landslide area within that parameter range to the percent of

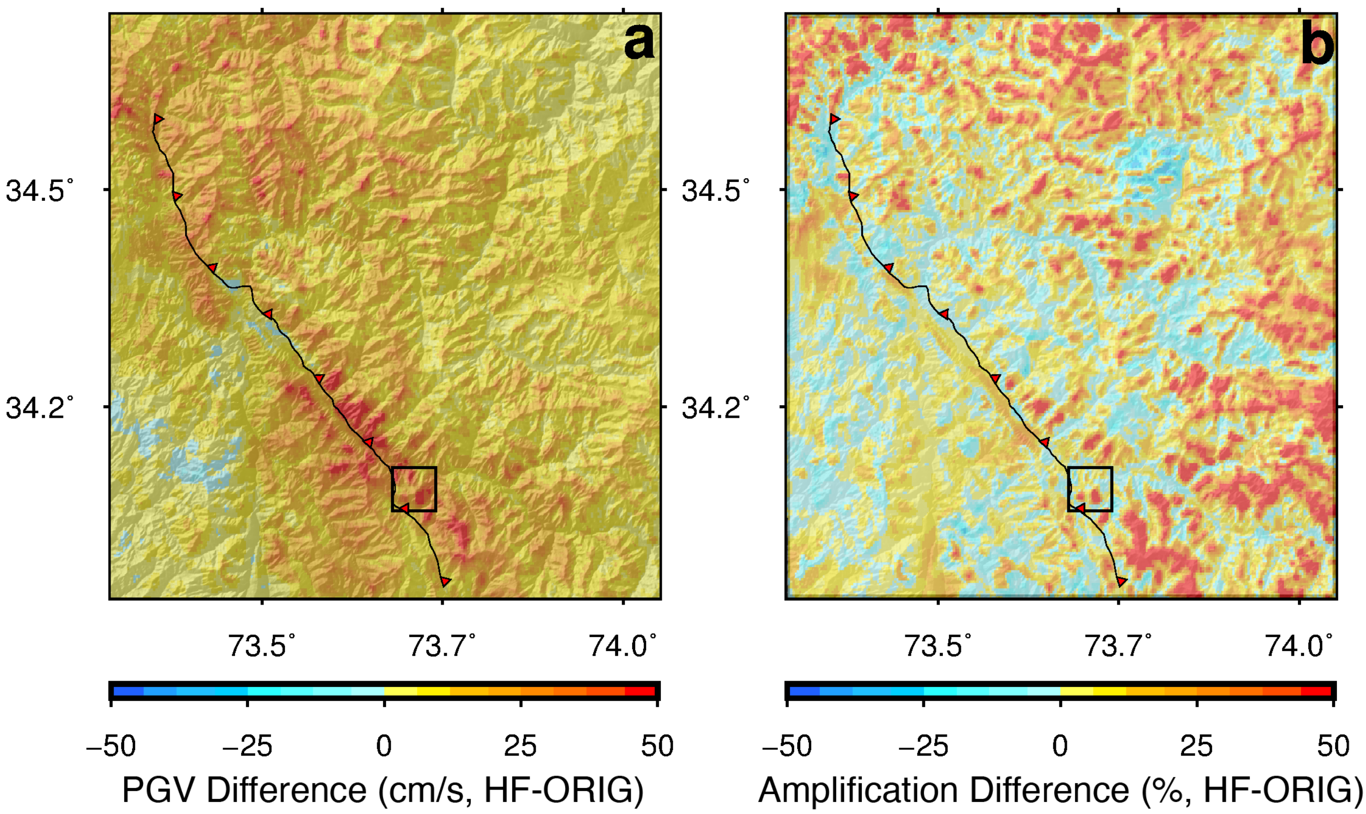

Figure 6 Difference between ORIG and HF for **(a)** PGV and **(b)** PGV topographic amplification. Line denotes surface rupture and box outlines Dana Hill, the location of the Hattian Bala landslide.

the total landslide area. Chung and Fabbri (2003) define values of R_{eff} > 3 as significant positive predictors of landslide occurrence and R_{eff} < 0.2 as significant negative predictors of landslide occurrence. We use this to compare the predictive capability of PGV and amplification for ORIG and HF as well as slope, elevation, local relief, distance to mapped faults, normalized distance to rivers, and lithology. The ratio of effectiveness is defined for each landslide parameter within 6 equally spaced ranges, bounded by the minimum and maximum values within the landslide database. Fig. 7 shows the predictive power of each parameter (R_{eff}), where the width of the bar is the range in which the ratio was calculated. Fig. 8 shows how each variable is distributed in space relative to the landslide database.

PGV values for both ORIG and HF show that the largest three categories have positive landslide prediction capability (R_{eff} >3), where PGV is greater than 68 cm/s and 80 cm/s for ORIG and HF, respectively. We clearly see that ORIG has higher predictive capability overall compared to HF, which is likely due to how we have calculated HF, generating higher amplitude shaking at the down dip portion of the rupture where there are relatively fewer landslides, explaining the decrease in the predictive power of large PGVs for HF compared to ORIG. Although we show that PGV from ORIG has a higher predictive capacity than HF, we will be using PGVs from HF for the remainder of the results and discussion, as it likely represents a more realistic source with rise times varying with slip and depth and is a better match to the USGS ShakeMap. No category of amplification for either ORIG or HF has significant positive predictive power (R_{eff} > 3); however, this could be because our ground motion simulations contain relatively low frequencies (< 2.7 Hz). This catalog comprises many small landslides initiating on smaller topographic features than we expect to see amplified by the frequencies in our simulations. This could also be related to the fact that high topographic amplification does not signify high absolute ground motions, which is a positive predictor of landslide occurrence, meaning that amplifications alone are not reliable predictors.

No local relief or elevation category exceeds R_{eff} >3, meaning that they do not show any significant positive predictive capacity of landslide initiation. Slopes in the largest two categories, > ~46°, show an increasing positive control on landslide predictability, demonstrating that slope is the most important topographic parameter evaluated in terms of landslide initiation. Slopes below ~17° also show a negative predictive capacity (R_{eff} < 0.2), indicating that landslides are unlikely to occur on slopes below this threshold angle.

Distance to faults and rivers, as well as lithology, are also important parameters that affect landslide initiation, particularly for this earthquake (Kamp et al., 2008; Sato et al., 2007). Within 1000 m of a fault, there is significant positive predictability of landslide initiation. For the 2005 Kashmir earthquake, faults increase landslide susceptibility in two ways: (1) decreased rock strength due to rock damage from the localized strain of the fault zone, and (2) concentration of peak ground shaking along the causative fault of the earthquake (Massey

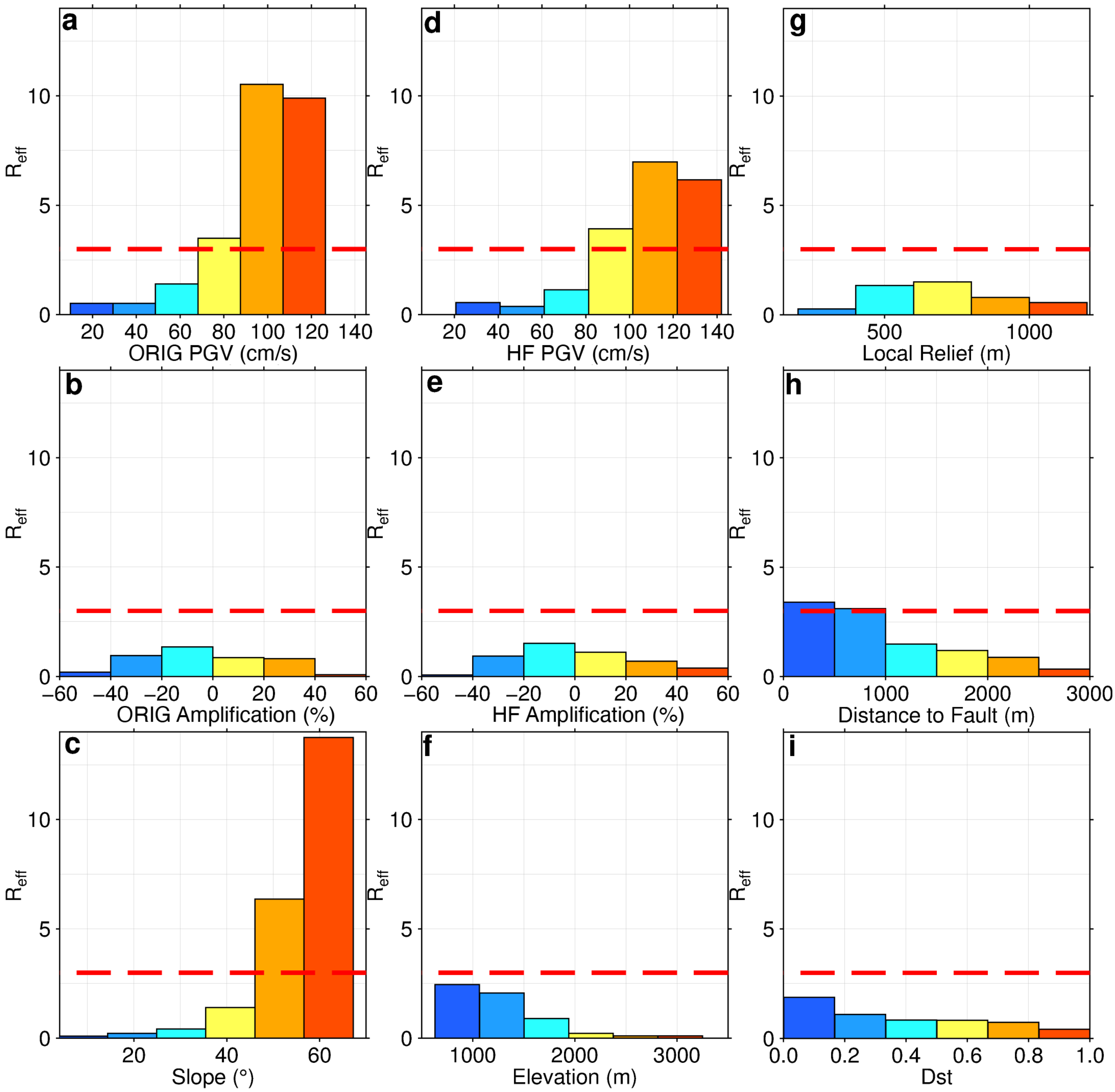

Figure 7 Predictive capacity of different parameters affecting landslide initiation. **(a)** Horizontal PGV for ORIG, **(b)** horizontal PGV Amplification for ORIG, **(c)** slope, **(d)** horizontal PGV for HF, **(e)** horizontal PGV Amplification for HF, **(f)** elevation, **(g)** local relief, **(h)** distance to mapped faults, and **(i)** d_{st} or normalized river distance. Colors show the lowest to highest valued categories for each parameter in blue to red, respectively. Y-axis is the same for all parameters, defined by the parameter with the highest value of R_{eff}, slope. Red dashed line denotes a R_{eff} value of 3.

et al., 2018). The normalized distance to rivers (d_{st}) shows values R_{eff} <3, meaning this is not a significant positive predictor of landslide occurrence. We also calculated R_{eff} for the lateral distance to major rivers in the region, finding all values of R_{eff}<3, providing further evidence that rivers are not the main drivers of the overall area of landsliding from this earthquake. Because we see high concentrations of landslides in the major river systems (see Discussion section *Landslides not located along the surface rupture*), this may indicate that rivers host smaller landslides than other regions and therefore do no act as a good predictor of landslide area with the R_{eff} metric. We also calculate R_{eff} for different geologic units and find that the Muzaffarabad Fm is the only geologic formation with any predictive capacity with R_{eff} ~14. This is because this formation covers relatively little area but hosts most of the landslide area from the earthquake.

5.5 Landslide location along the hillslope

Using R_{eff}, we show that the normalized river distance, d_{st}, is not a positive predictor of landslide initiation, meaning that the overall landslide area is not focused at either ridges (d_{st} = 1) or rivers (d_{st} = 0). We examine the spatial distribution of crest clustering using Rp_{crest}, a

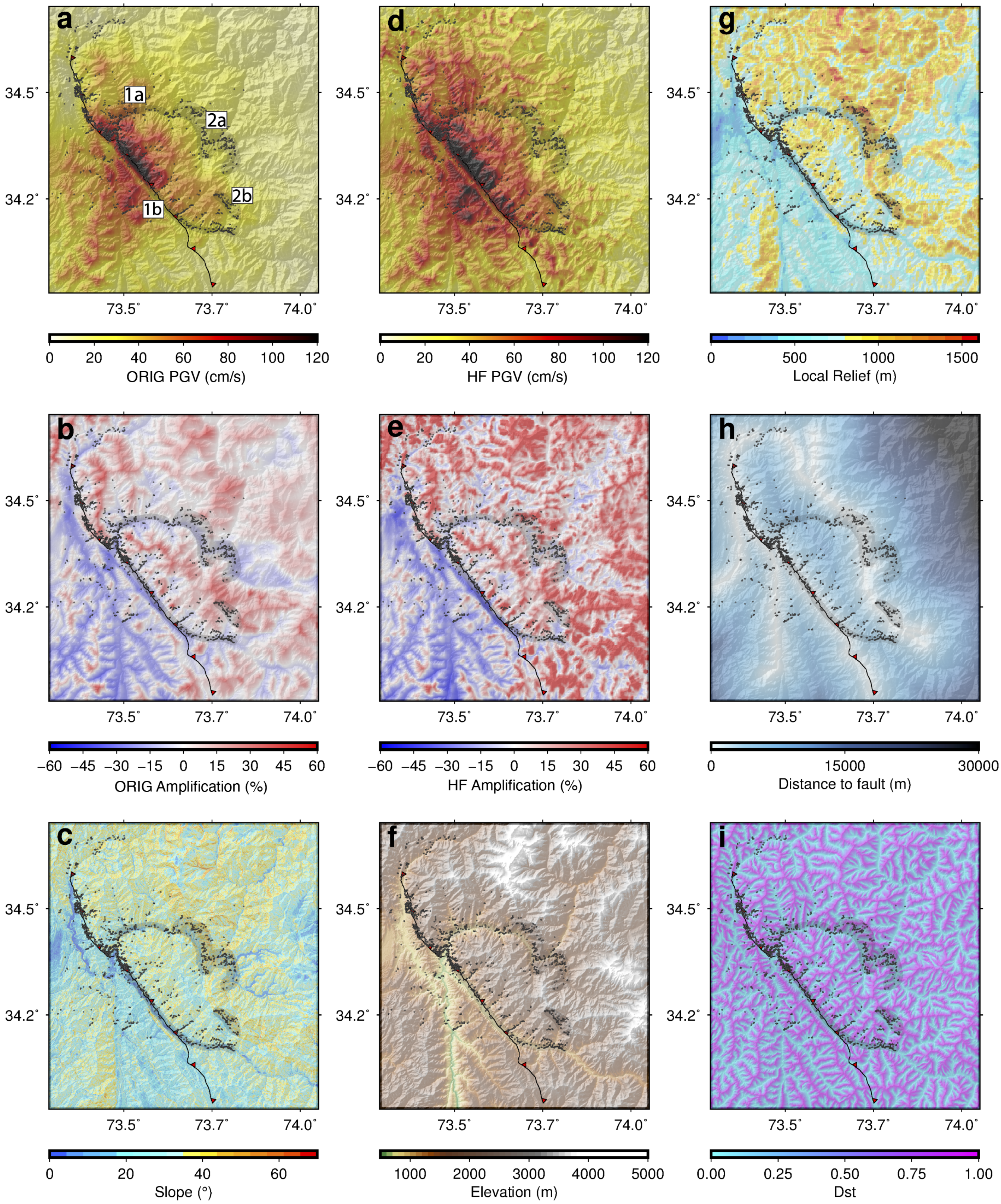

Figure 8 Spatial distribution of landslides in different variables affecting landslide occurrence, **(a)** Horizontal PGV for ORIG, **(b)** horizontal PGV Amplification for ORIG, **(c)** slope, **(d)** horizontal PGV for HF, **(e)** horizontal PGV Amplification for HF, **(f)** elevation, **(g)** local relief, **(h)** distance to mapped faults, and **(i)** d_{st} or normalized river distance. Transparent polygons represent regions of landsliding discussed in the text. **1a/b** are landslides within river valleys and **2a/b** are landslides along faults on the eastern limb of the HKS.

variable that denotes crest ($Rp_{crest} \gg 1$) or toe ($Rp_{crest} \ll 1$) clustering of landslides in designated regions (see Supplementary Text S2 for expanded discussion of Rp_{crest}) (Rault et al., 2019). Fig. 9a shows Rp_{crest} for 4.5 km x 4.5 km "macrocells", with warm colors denoting crest clustering and cool colors denoting toe clustering (see Supplementary Fig. S5 for testing of other macrocell sizes). Maps of Rp_{crest} show that toe clustering is the predominant mechanism of landslide initiation from this earthquake. Examples of this toe clustering include the Neelum (Figs 9a, 1a) and Jhelum River (Figs 9a, 1b) valleys, and examples of crest clustering can be seen at the Neelum River mouth (Fig. 9a, 3), where the river intersects the surface rupture and the Muzaffarabad Fm and at the eastern edge of the Neelum River (Figs 9a, 2a) and within rocks of the Hazara Fm (Figs 9a, 2b) to the south. Even within these highlighted regions, only a small portion of the macrocells exhibit crest clustering.

To understand the relationship between crest clustering and topographic amplification, we plot the average value of topographic amplification grid points within each 4.5 km x 4.5 km macrocell (Fig. 9b) and compare Rp_{crest} and average amplification in Fig. 9c. There is no strong relationship between topographic amplification and crest clustering, with few macrocells exhibiting both positive amplification and crest clustering. This indicates that, at this scale and frequency content (<2.7 Hz), crest clustering of coseismic landslides does not signify the initiation mechanism of topographic amplification. It also shows that, on average and at this macrocell scale, topographic amplification is dominant on the hanging wall but not on the footwall.

5.6 Landslide frequency-area distribution

Frequency-area distributions (FADs) for landslide catalogs exhibit a power law relationship that shows the relative frequency of large and small landslides. We calculate FADs and power law exponents (α) for five different categories of the landslide database, positively or negatively amplified (Fig. 10a), steep (>40°) or gentle (<40°) slopes (Fig. 10b), high (>80 cm/s) or low (<80 cm/s) PGV (Fig. 10c), high (>1500 m) or low (<1500 m) elevation (Fig. 10d), and within or outside of the Muzaffarabad Fm (Fig. 10e). See Supplementary Text S3 for a complete methodology for calculating FADs and α. For the ground shaking parameters, we plot the FADs for HF, noting that ORIG does not demonstrate a significant difference in the FAD from HF. Larger values of α (more negative) indicate a lower frequency of larger landslides and smaller values of α (less negative) indicate a higher frequency of larger landslides. Higher frequencies of larger landslides are shown within positively amplified regions, high PGVs, steep slopes >40°, and within the Muzaffarabad Fm. Although a smaller α indicates that positive amplification has a higher frequency of larger landslides, because the difference in α between positively and negatively amplified landslides is much smaller than in other categories we do not interpret this as a strong control on landslide size. Elevation does not show any control on landslide area, with both high and low elevations having similar values of α.

5.7 Hattian Bala landslide analysis

From the amplification maps in Figs 5b and 5d, the causative slope of the Hattian Bala landslide is amplified by both ORIG and HF, but has higher ground shaking and amplification from HF. This leads us to conclude that the stronger ground motions and increased amplification of the causative slope is caused by higher frequency seismic waves not being emitted by ORIG. Although our simulations are only validated for HF, we are comparing the patterns of amplification to ORIG to understand how the differences in the source are impacting differences in amplification. The high ground shaking and amplification is most prominent on the side of the ridge facing away from the direction of the propagating wavefield, coincident with the location of preexisting failure (Dunning et al., 2007).

To estimate resonant frequencies of the hill that hosted the Hattian Bala landslide, we use Eq. 3 from Paolucci (2002):

$$f_t = \frac{V_S}{L} \tag{3}$$

Here, V_s is the shear velocity of our simulations, ~1500 m/s within the upper 1km, and L is the width of the hill, 1.5-3.5 km (~145° azimuth). Using these values, we find $f_\perp = 0.43 - 1$ Hz. We can also define L to be the length of the hill, ranging from 4.5-7 km (~55° azimuth), so that $f_\parallel = 0.2 - 0.3$ Hz. The asymmetry and irregularity of this hill give us these ranges in distance values. Because the frequency content of ORIG is dominant <0.75 Hz, these simple calculations indicate that ridge-perpendicular amplification may have been limited in the ORIG case which would explain the relatively weak amplification of the causative slope.

To determine what frequency is being amplified at different positions along the hillslope, we calculate standard spectral ratios (SSRs) at locations along the hill as compared to a reference station at the base of the hillslope. The SSR is a widely used tool, specifically to estimate the frequency of amplified ground shaking, typically compared to a reference station at the base of the topographic feature with the assumption that it is not affected by topographic amplification (Borcherdt, 1970; Massa et al., 2014; Rault et al., 2019; Héloïse et al., 2011). To calculate the SSR for each select station, we compute the Fourier amplitude spectra of the signals for both the reference station and station of interest from the topography simulations after applying a lowpass filter to 2.5 Hz and a 5% cosine taper. We then smooth the spectra using the Konno-Ohmachi method with a bandwidth coefficient b = 40 (Konno and Ohmachi, 1998). The SSR is calculated using:

$$SSR = \frac{S_t}{S_r} \tag{4}$$

where S_t is the Fourier spectrum of the topography station and S_r is the Fourier spectrum of the reference station. To determine any azimuthal variation in amplification, we rotate the horizontal components at 10° increments and calculate the SSR in each direction.

First, we can compare the SSR ratios from ORIG and HF at two stations at the top and middle of the landslide

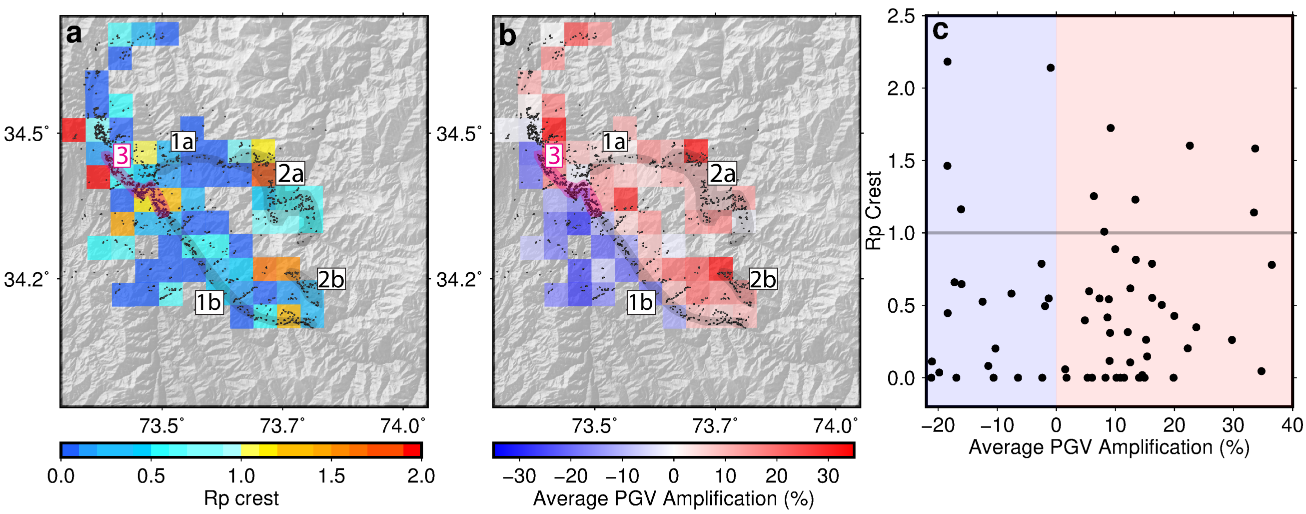

Figure 9 **(a)** Calculated Rp_{crest} values for 4.5 km x 4.5 km macrocells. **(b)** Average PGV amplification within each 4.5 km x 4.5 km microcell. **(c)** Scatter plot comparing the average PGV amplification and Rp_{crest} values within the macrocells shown in a and b. Red indicates amplified and blue indicates de-amplified. The horizontal gray line denotes the separation between toe clustering (< 1) and crest clustering (> 1). a and b show annotations: **1a/b** are landslides within river valleys, **2a/b** are landslides along faults on the eastern limb of the HKS, **3** are landslides at the mouth of the Neelum river valley. 3 is highlighted in pink as it is the only segment not shown in Fig. 8.

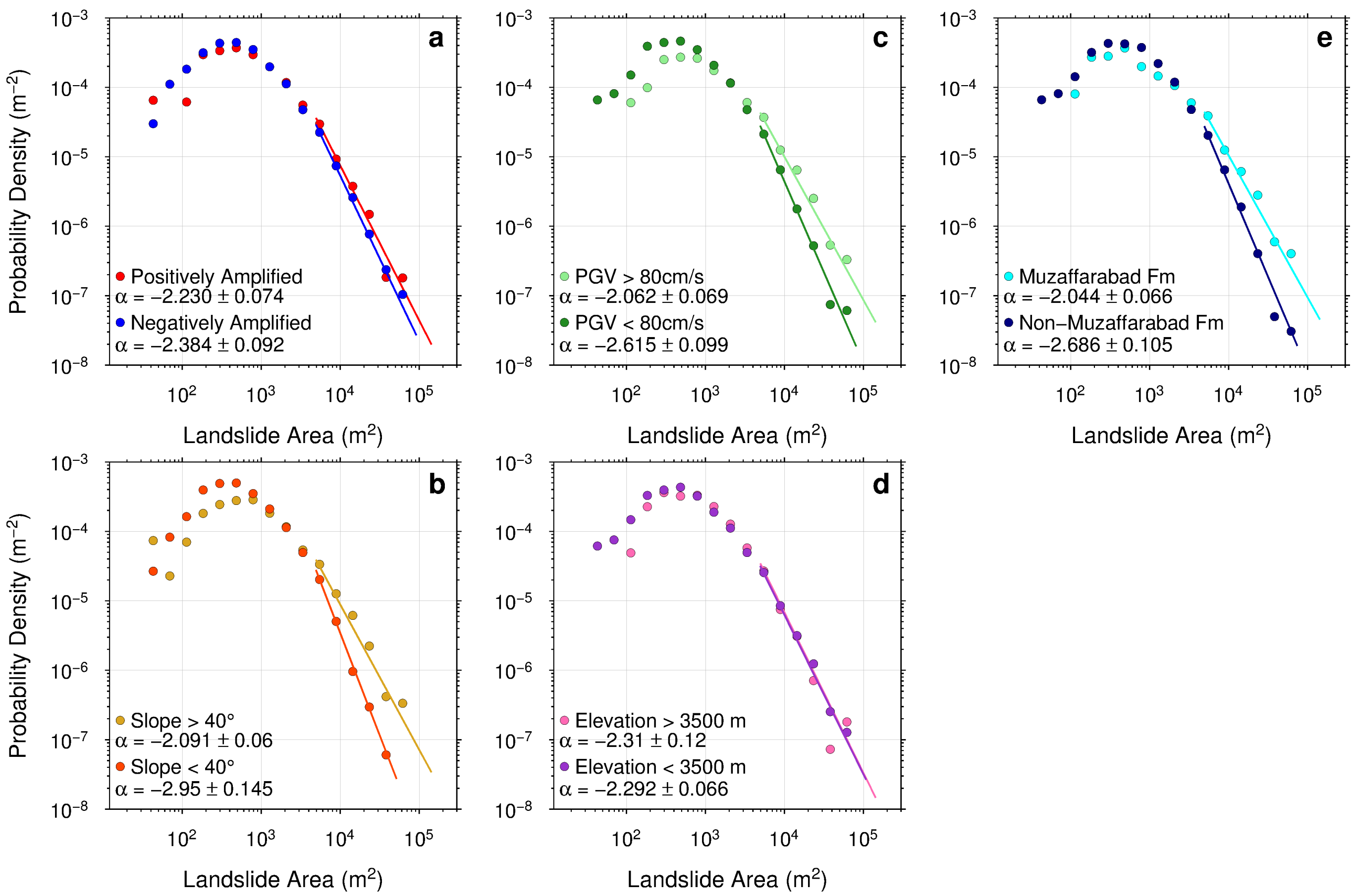

Figure 10 Landslide frequency-area distribution (FADs) for subsets of the landslide database. **(a)** Positively (N = 1160) or negatively (N = 1252) amplified landslides, **(b)** landslides on slopes > 40 ° (N = 1019) and < 40° (N = 1402), **(c)** landslides with PGV > 80 cm/s (N = 1019) and < 80 cm/s (N = 1402), **(d)** landslides at elevations > 1500 m (N = 582) and < 1500 m (N = 1839), **(e)** landslides within (N = 714) and outside (N=1707) of the Muzaffarabad Fm. N is the number of landslides used to calculate each category.

(Fig. 11). HF has moderately higher SSRs (increased amplification) and similar patterns compared to ORIG at frequencies < 1Hz, but amplifications > 1 Hz are only present in HF. Both ORIG and HF demonstrate higher amplitudes for SSRs at the middle compared to the ridge top, providing further evidence that we have strong shaking and amplification not just at the ridge top, but throughout the slope where the landslide initiated (up to 120% for HF). The increased frequency content of HF allows for the amplification of smaller scale features of the ridge compared to ORIG.

To understand the polarization of these various frequency bands for HF, we plot SSRs for stations along the ridge axis (Fig. 12), showing that the polarization of amplification at the ridge top is perpendicular to the ridge axis, rotating with the curve of the ridge from approximately N-S to NNW (black and white lines). This indicates a clear dependence of amplification on the orientation of the ridge. Along the west limb of the ridge (Fig. 12), the amplification is polarized approximately perpendicular at frequencies between ~0.5-1 Hz, which aligns well with a ridge width of ~1.5-2.5 km and Vs = 1.5 km/s. Along the east limb of the ridge (Fig. 12), the amplification is again polarized in the ridge perpendicular direction at similar frequencies due to a similar ridge width (~2-2.5 km).

6 Discussion

6.1 Landslides along the surface rupture

The predictive capacity of various parameters has shown that PGV, slope, fault distance, and lithology were the primary drivers of landslide initiation during the Kashmir earthquake. These findings align with previous studies that investigated the geomorphic and geologic controls on Kashmir earthquake landsliding (e.g., Kamp et al., 2008; Khattak et al., 2010; Owen et al., 2008; Shafique, 2020; Khan et al., 2013), and expand upon these investigations using simulated ground motions to show the influence of high PGVs on coseismic landslide initiation. Studies of coseismic landslide distributions from other earthquakes have also found that landslides concentrate along the surface rupture, primarily as a function of strong peak ground shaking close to the surface trace. Examples of this have been shown for the 2002 Denali earthquake (Gorum et al., 2014), 2008 Mw 7.9 Wenchuan earthquake (Xu et al.), the 2016 Mw 7.8 Kaikōura earthquake (Massey et al., 2018), and most recently the 2023 Türkiye earthquake sequence (Görüm et al., 2023). These parameters are all interrelated, with the highest PGVs, some of the steepest slopes, and the most susceptible geologic unit (the Muzaffarabad Fm), all located along the surface rupture. To explore these relationships, Fig. 13 shows how the landslide area density, landslide frequency, and PGV vary along the surface rupture. These curves are generated by taking the sum of the area of all landslides, number of landslides, and average PGV within 1 km laterally spaced bins. Landslide frequency is a percent of the total number of landslides in the database and landslide area is a percent based on the total area of each bin, which are equal between bins. This region is divided into landslides occurring dominantly within the Muzaffarabad Fm to the north (I) and within the Murree Fm and Quaternary alluvium to the south (II). At the northern end of the surface rupture (I, 0-10 km), landslides are focused within the Muzaffarabad Fm and have a high landslide frequency but a low landslide area density, meaning that in this region there are many small landslides. PGV values are at their lowest along the surface rupture (25-50 cm/s). Shifting farther south (I, 10-17 km), landslide frequency decreases with an increase in landslide area density, showing that there are fewer landslides, but these landslides are typically larger. PGVs are steadily growing but are in the range of 50-100 cm/s. Even farther south (I, 17-26 km), we see the highest landslide area density and frequency, still within the Muzaffarabad Fm, specifically near the mouth of the Neelum River, where PGV values are ~120 cm/s here. The transition between the Muzaffarabad Fm to the north and the Murree formation to the south (~26 km) shows a steep decline in both landslide area density and frequency with continually increasing PGVs that reach their highest value for the earthquake, ~125 cm/s. Slopes in both (I) and (II) have very similar distributions, with modal slopes of 31° and 32.5°, respectively. This means that the variation in landslides between the north and south is likely not due to differences in slope distribution. We also note that there were pre-earthquake landslides within the Muzaffarabad Fm (cyan polygons, Shafique, 2020), demonstrating the overall landslide susceptibility of this unit as well as the potential for past landslide deposits to increase coseismic landslide susceptibility. The cause of the variation in landslide frequency and area density along the surface rupture is likely due primarily to lithology because the other positive predictors of landslide occurrence (PGV, slope, distance to faults) remain relatively constant.

To investigate how these variables affect landslide initiation and size, we focus on landslides just within the Muzaffarabad Fm to isolate the effects of both lithology and distance to the surface rupture on landslide initiation. To do this, we separate the Muzaffarabad Fm into northern (Fig. 13, I. 0-10 km, dark pink) and southern regions (Fig. 13, I. 10-26 km, light pink), which were shown above to have increasing landslide area density from north to south with landslides covering 4% and 15% of each region, respectively. Using FADs, we show that landslide distributions within regions of high PGVs, steep slopes, and within the Muzaffarabad Fm have a higher frequency of larger landslides (Fig. 10). The north clearly has lower PGV values compared to the south, aligning with a decrease in landslide area density and size. To quantify how slope angles relate to landsliding in the northern and southern regions, we compare the slope distributions of the landslides (P_L) to the slope distributions of the topography (P_T) to define an over or under sampling of the topographic slopes by landslides (full methods described in Dunham et al., 2022; Marc et al., 2018) (Fig. 14). The distribution of slopes within the topography of the southern section has a larger modal slope (Fig. 14a, light pink solid line) as well as a higher magnitude of steep slope oversam-

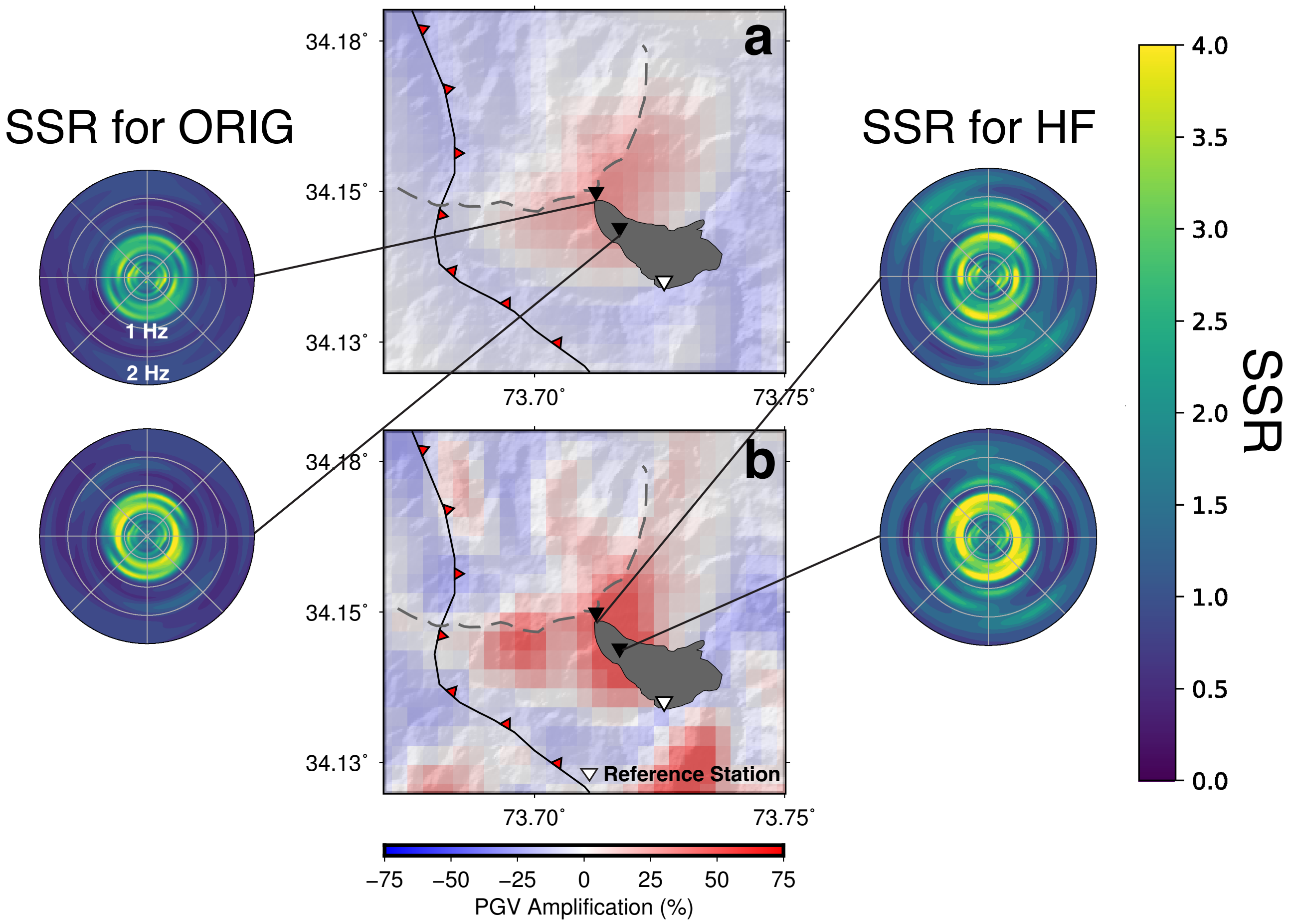

Figure 11 Polar plots of SSR for **(a)** ORIG and **(b)** HF for 2 stations at the ridge and middle (black triangles) compared to the reference station (white triangle) at the base. Maps show a zoom-in on causative slope of Hattian Bala landslide with PGV amplification for (a) ORIG and (b) HF, gray dashed line is the ridge top, gray polygon is the Hattian Bala landslide from (Basharat et al., 2016). Black line with red triangles is the surface rupture. Polar plots show SSR at varying azimuths (N=0°) and radial direction denotes frequency at 0.5 Hz increments.

pling (Fig. 14b, light pink line) compared to the northern section. This means that the southern section has more available steep slopes and an increased sampling of landslides on those steep slopes. This leads us to conclude that the lower PGV values and gentler slopes in the north contribute to the lower concentration of larger landslides compared to landslides in the south, where there are higher PGVs and steeper slopes. Landslide size and initiation in the south is also likely affected by proximity to the Neelum River, generating steeper slopes and potentially higher susceptibility to landsliding due to river incision (Owen et al., 2008). By isolating the impacts of lithology and fault distance on landslide initiation, we show that both higher PGVs and steeper slopes cause the initiation of larger landslides, while gentler slopes and lower PGVs are responsible for triggering a similar frequency of smaller landslides, highlighting the interdependence of both slope and absolute ground shaking on landslide size.

6.2 Landslides not located along the surface rupture

Although most of the landslides and landslide area are focused along the surface rupture, this is not the only region where landslides initiated during the earthquake. It is clear that there are two main zones of landsliding aside from the surface rupture, the Neelum (Figs 8, 1a) and Jhelum (Figs 8, 1b) River valleys and the thrust faults along the eastern limb of the HKS (Figs 8, 2a, 2b). These locations experienced comparatively smaller ground shaking than at the surface rupture but likely were predisposed to landsliding due to their locations within river valleys and along faults, evidenced by a history of landsliding due to other triggering mechanisms (Sarfraz et al., 2023). We note that these regions could have experienced higher amplitude ground shak-

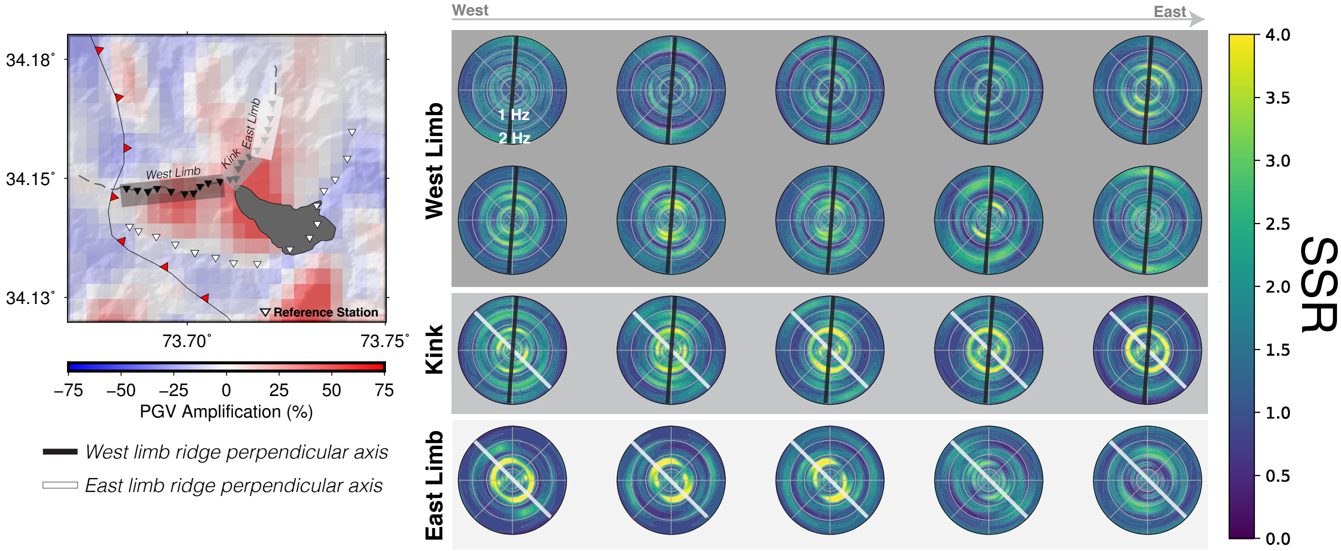

Figure 12 Amplification for various locations along the causative ridge of the Hattian Bala landslide. Map shows topographic amplification from HF. Gray dashed line is the ridge top, gray polygon is the Hattian Bala landslide from (Basharat et al., 2016). Stations are inverted triangles, black stations are observations and white stations are reference. Polar plots are associated with stations going from west to east, labels and black, gray, and white shaded regions denote the west limb, kink, and east limb of the ridge, respectively. For the west limb panel, the top row shows the westernmost stations and the bottom row shows the easternmost stations. Colors denote SSR for azimuth and frequency content (0.5 Hz radial intervals). Black and white lines show the approximate direction perpendicular to the ridge axis for west limb and east limb, respectively.

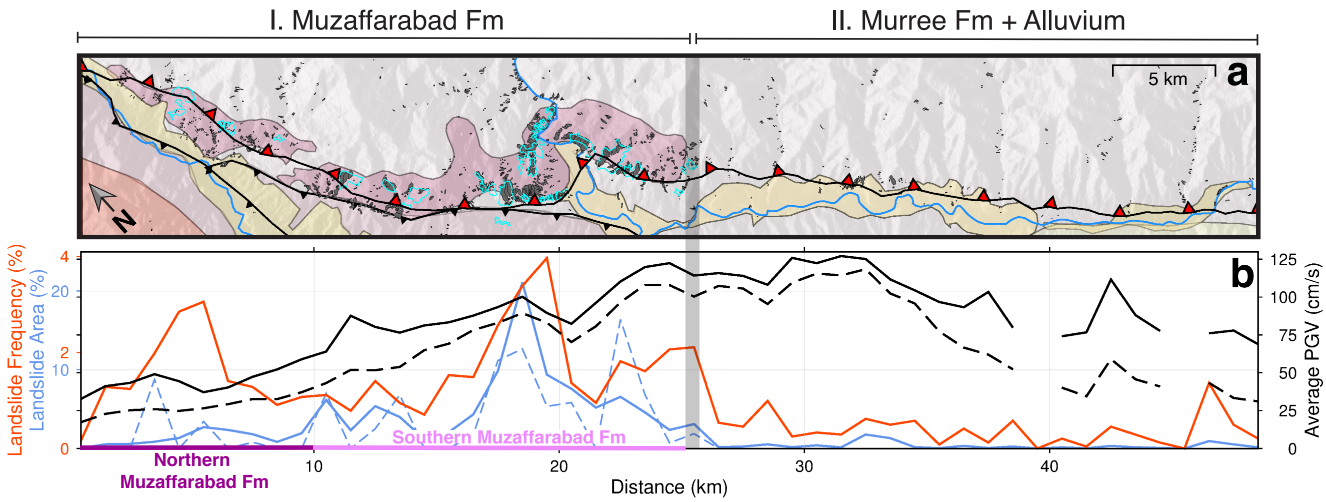

Figure 13 **(a)** Landslides along the surface rupture of the earthquake (black line with red triangles). Coseismic landslides are gray polygons from (Sato et al., 2007). Outlines of pre-earthquake landslides from 2004 15 m ASTER imagery shown in cyan (Shafique, 2020). These were only mapped within the Muzaffarabad Fm. **(b)** Averages of landslide frequency (red line), landslide area density (blue line), and peak ground velocity (ORIG – black dashed line, HF – black solid line) along the surface rupture. Regions with a broken line means that there are no landslides within that bin. Blue dashed line denotes the landslide area frequency of pre-earthquake landslides from (Shafique, 2020). Dark and light pink regions denote the northern and southern Muzaffarabad Fm, respectively.

ing than modeled here due to the amplifying effect of lower velocity quaternary sediments present in river valleys. There are also reported anthropogenic causes of landslides along the major road in the Neelum Valley (Owen et al., 2008; Sarfraz et al., 2023). Fig. 8h shows the distance to large, mapped faults in the region, with light blues/whites denoting closer distances and dark blues/blacks denoting farther distances. Landslides in these zones (2a/b) are clustered in Hazara and Salkhala units and exhibit some crest clustering (Fig. 9a) as well as some effects of topographic amplification (Fig. 9b), particularly zone 2b. The Hazara Fm is highly cleaved and fractured and exhibits high landslide susceptibility near faults and rivers, even on the footwall, where

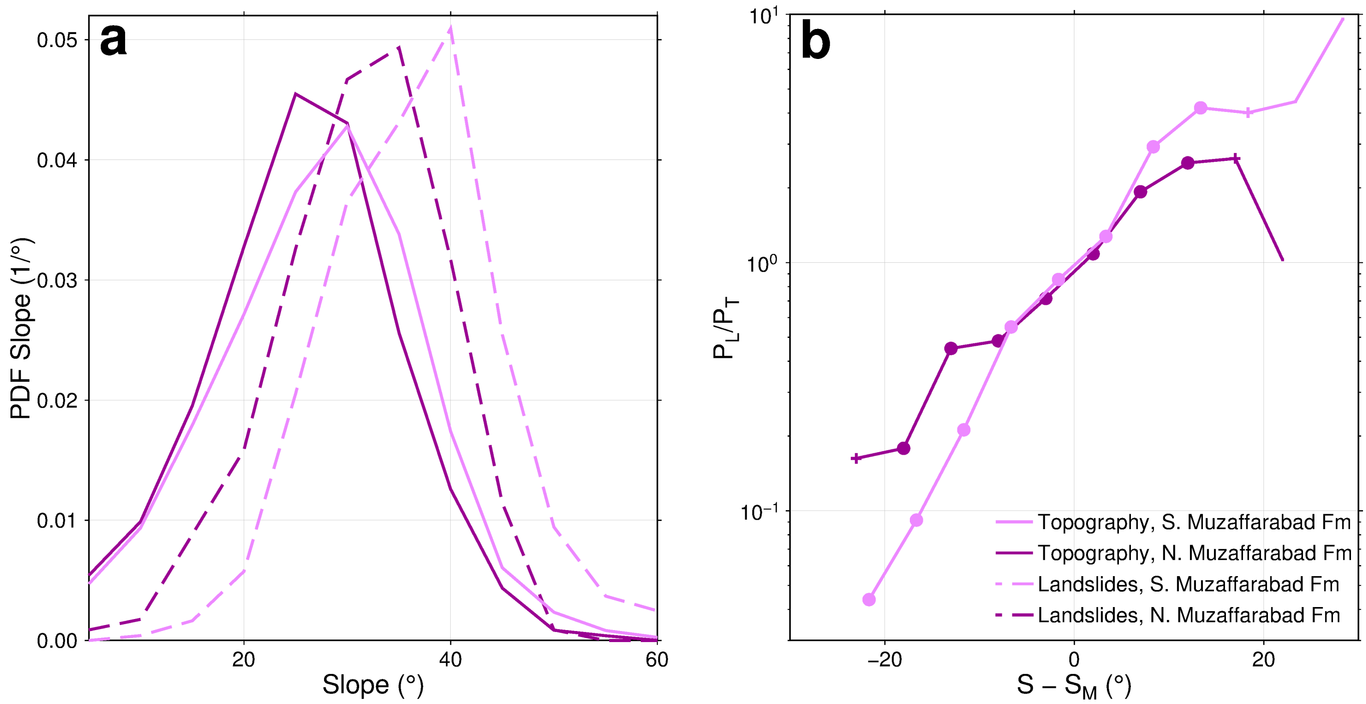

Figure 14 **(a)** Probability density functions (PDF) of slopes for the topography within the northern and southern Muzaffarabad Fm, dark and light pink solid lines, respectively, and the slope distributions for landslides within the N and S Muzaffarabad Fm, dark and light pink dashed lines, respectively. **(b)** Probability density ratio (P_L/P_T) of landslide slope distribution and topography slope distribution compared to S-Sm which is the slope minus the slope mode (Sm) of topography. Circles denote points that are within a 95% confidence interval and crosses indicate bins that do not have sufficient samples to evaluate.

there is comparatively lower shaking than the hanging wall (Owen et al., 2008). Landslides in 2b are also topographically amplified (Fig. 9b) and larger than those that initiate within the river valleys (1a/b), indicating a slight control of topographic amplification on landslide size.

We also see some landslides located within the Murree Fm that are far from any river or fault that may cause a predisposition to failure. Much of the Murree Fm is dominated by low amplitude ground motions away from the surface rupture. Because these landslides are located within the core of the HKS, we might expect less deformation farther from faults and, therefore, stronger, more coherent rocks, less likely to produce ground failure unless there is significant ground shaking. Topographic amplification is not a positive predictor of landslide occurrence but could affect landslide initiation in select cases, particularly when there are no other obvious predispositions to landslide occurrence. To see what effect amplification had on landslide initiation within the Murree Fm without influence from other factors, we took all the landslides within the Murree Fm that were >1000 m from a fault (past where faults are a positive predictor of landslides) and >1/3 up a hillslope from a river, chosen to indicate that above this value, hydrologic effects in the valley below would have limited influence on landslide occurrence. Of these, 73% of landslides experience topographic amplification (from HF), compared to the background topography that is 62% amplified overall. This shows that when not considering other predisposing factors, topographic amplification has a control on landslide initiation. This aligns with the findings of Rault et al. (2019) that topographic amplification can play a role in rocks with little deformation and no significant lithologic variability.

6.3 Hattian Bala landslide

Using SSRs, we examine the topographic amplification across the causative ridge of the Hattian Bala Landslide. While it is clear that this ridge was experiencing deformation prior to the earthquake that led to failure (Dunning et al., 2007), we can use these simulations to conclude if topographic amplification of the causative ridge occurred and therefore could have contributed to landslide initiation. We see some of the highest amplifications within the ridge kink, which experienced amplification from both the east and west limb ridge perpendicular directions (Fig. 12). This transition in amplification is clear across these stations and likely results in the higher amplifications due to wave focusing within this kink. This kink is also where the Hattian Bala landslide initiated. There is a small fraction (~250 m) of the ridge length that is experiencing this multi-directional and multi-frequency amplification and this could cause increased risk of landslide occurrence. This kink likely causes energy to get trapped within this shorter wavelength feature in the topography, increasing these amplifications at some higher frequencies (~1.5 Hz) as well compared to stations located on sections of the ridge that do not change direction (illustrated in Fig. 15). Increased amplification at a kink in the ridge was also shown for the source area of the Langtang Valley land-

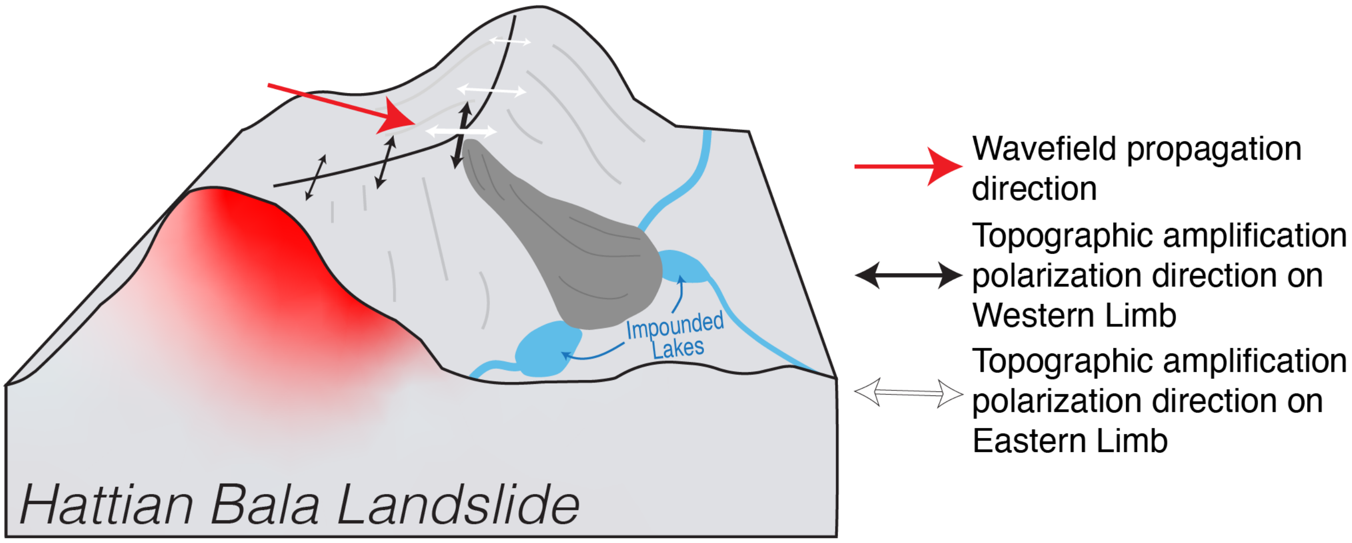

Figure 15 Cartoon showing the polarization directions of topographic amplification across the causative ridge of the Hattian Bala landslide. Red region denotes highest topographic amplification of the ridge side facing away from the propagation direction. Thicker black and white arrows denotes higher amplification compared to thinner arrows.

slide (Dunham et al., 2022), the largest and most devastating landslide caused by the 2015 Gorkha earthquake in Nepal. By modeling topographic amplification of ridge features in California, Asimaki and Mohammadi (2018) also showed this phenomenon by demonstrating that topographic amplification is higher where ridges with differing azimuths intersect (i.e. at a kink). The Daguangboa landslide, the largest landslide triggered by the 2008 M_W 7.9 Wenchuan earthquake, was similarly positioned to the Hattian Bala landslide, both on the hanging wall, close (~6.5 km) to the surface rupture, and with the slope failure facing in the direction of rupture propagation (Huang et al., 2011). It has been speculated that topographic amplification was a factor in initiating this large landslide but there were no seismic recordings to confirm this (Huang et al., 2011). The pre-earthquake imagery of the topography shows ridges with multiple azimuths converging at the head scarp, making it a potential candidate to investigate this phenomenon further. To first order, we show that the amplification of a topographic feature is controlled by the fundamental frequency of the feature and the orientation and frequency content of the wavefield. It is also clear that smaller features within a larger ridge are essential to the overall amplification pattern and focusing of seismic waves. While we have identified two locations (the Langtang and Hattian Bala landslides) where the seismic wavefield from a large earthquake interacted with a topographic kink to produce enhanced topographic amplification accompanied by a large coseismic landslide, future studies to comprehensively document and model this effect are necessary, such as for the Daguangboa landslide.

6.4 Implications for coseismic landslide hazard assessment

Current frameworks for assessing post-earthquake landslide hazards rely on products such as the USGS ShakeMap that do not include the effects of topography, and in mountainous regions, typically have limited observational shaking data (Allstadt et al., 2018; Nowicki Jessee et al., 2018). While simulations, such as the ones in this study, can be computationally costly, limited in frequency content, and rely on regionally specific information that is not always available (i.e. high-resolution 3D velocity models), they provide time-dependent information, beyond simplified intensity measures, that could be leveraged along with machine learning approaches to improve real-time estimates of coseismic landslide distributions (Dahal et al., 2024). As computational costs continue to decrease, future research could focus on developing regional velocity models validated to higher frequencies in these mountainous regions to explore the possibility of using simulations in real-time landslide hazard assessment tools. We have also highlighted here particular locations of interest where coseismic landslides are most likely to occur, such as steep slopes, susceptible lithology, near faulting, and sites that may experience high PGVs. While PGV, lithology, and slope are currently included in the rapid assessment of earthquake triggered landslides (Nowicki Jessee et al., 2018), more detailed regional assessments including mapped faults could improve estimates of coseismic landslide distributions.

7 Conclusions

Here, we use the simulation of ground motions and topographic amplification, along with topographic and geologic parameters, to investigate the distribution of landslides and landslide size from the M_w 7.6 2005 Kashmir earthquake. We found that lithology, high PGVs, topographic slope, proximity to faulting and to a lesser extent rivers, and lithology are all important variables for landslide initiation from this earthquake. Landslide size is most strongly controlled by high PGVs, steep slopes, and occurrence in the Muzaffarabad Fm. Although the Hattian Bala landslide was likely promoted by pre-existing weakness, we found that positive topographic amplification is focused at the location of landslide initiation, oriented perpendicular to both limbs of the ridge at frequencies ranging from 0.5-2 Hz (Fig. 15), likely due to the trapping of energy within the ridge kink, illustrating that smaller-scale modeling efforts are necessary to fully understand this phenomenon and how it relates to the initiation of large coseismic landslides.

Acknowledgements

We would like to thank Erin Wirth and alex grant for their helpful comments as well as the editor and two anonymous reviewers. This study was supported by the NASA Interdisciplinary Science program, grant 80NSSC18K0432. CSW was supported by the UKRI GCRF Urban Disaster Risk Hub (NE/S009000/1) (Tomorrow's Cities), and the Centre for the Observation and Modelling of Earthquakes, Volcanoes and Tectonics (COMET). DHS was supported by NSER 2020-04207. Simulations were run on the High Performance Computing (HPC) resources supported by the University of Arizona TRIF, UITS, and Research, Innovation, and Impact (RII) and maintained by the UArizona Research Technologies department.

Data and code availability

Supplementary movies can be found at Dunham (2024). The data and software used in the simulations included (1) a finite fault model from Avouac et al. (2006), and can be found on SRCMOD (http://equake-rc.info/SRCMOD/searchmodels/viewmodel/HF005KASHMI01KONC/),
(2) 30 m topographic data that was provided by SRTM3 (Farr et al., 2007) and distributed by GMTSAR (https://topex.ucsd.edu/gmtsar/demgen/)(this topography was also used in the analysis), and (3) open source software SPECFEM3D cartesian (Komatitsch and Tromp, 2002a,b, distributed by Computational Infrastructure for Geophysics (https://geodynamics.org/resources/notebooks). The landslide database is from Sato et al. (2007) and is available from https://www.sciencebase.gov/catalog/item/5874bb46e4b0a829a320bb99.

Competing interests

The authors have no competing interests

References

Abrahamson, N. A. and Somerville, P. G. Effects of the hanging wall and footwall on ground motions recorded during the Northridge earthquake. *Bulletin of the Seismological Society of America*, 86(1B):S93–S99, Feb. 1996. doi: 10.1785/bssa08601b0s93.

Allstadt, K. E., Jibson, R. W., Thompson, E. M., Massey, C. I., Wald, D. J., Godt, J. W., and Rengers, F. K. Improving Near-Real-Time Coseismic Landslide Models: Lessons Learned from the 2016 Kaikōura, New Zealand, Earthquake. *Bulletin of the Seismological Society of America*, 108(3B):1649–1664, Mar. 2018. doi: 10.1785/0120170297.

Asimaki, D. and Mohammadi, K. On the complexity of seismic waves trapped in irregular topographies. *Soil Dynamics and Earthquake Engineering*, 114:424–437, Nov. 2018. doi: 10.1016/j.soildyn.2018.07.020.

Assimaki, D. and Jeong, S. Ground-Motion Observations at Hotel Montana during the M 7.0 2010 Haiti Earthquake: Topography or Soil Amplification? *Bulletin of the Seismological Society of America*, 103(5):2577–2590, Sept. 2013. doi: 10.1785/0120120242.

Avouac, J.-P., Ayoub, F., Leprince, S., Konca, O., and Helmberger, D. V. The 2005, Mw 7.6 Kashmir earthquake: Sub-pixel correlation of ASTER images and seismic waveforms analysis. *Earth and Planetary Science Letters*, 249(3–4):514–528, Sept. 2006. doi: 10.1016/j.epsl.2006.06.025.

Basharat, M., Rohn, J., Baig, M. S., and Khan, M. R. Spatial distribution analysis of mass movements triggered by the 2005 Kashmir earthquake in the Northeast Himalayas of Pakistan. *Geomorphology*, 206:203–214, Feb. 2014. doi: 10.1016/j.geomorph.2013.09.025.

Basharat, M., Ali, A., Jadoon, I. A. K., and Rohn, J. Using PCA in evaluating event-controlling attributes of landsliding in the 2005 Kashmir earthquake region, NW Himalayas, Pakistan. *Natural Hazards*, 81(3):1999–2017, Jan. 2016. doi: 10.1007/s11069-016-2172-9.

Basharat, M., Riaz, M. T., Jan, M. Q., Xu, C., and Riaz, S. A review of landslides related to the 2005 Kashmir Earthquake: implication and future challenges. *Natural Hazards*, 108(1):1–30, Mar. 2021. doi: 10.1007/s11069-021-04688-8.

Bilham, R. Himalayan earthquakes: a review of historical seismicity and early 21st century slip potential. *Geological Society, London, Special Publications*, 483(1):423–482, Feb. 2019. doi: 10.1144/sp483.16.

Borcherdt, R. Effects of local geology on ground motion near San Francisco Bay. *Bulletin of the Seismological Society of America*, 60(1):29–61, 1970.

Bourdeau, C., Havenith, H.-B., Fleurisson, J.-A., and Grandjean, G. *Numerical Modelling of Seismic Slope Stability*, page 671–684. Springer Berlin Heidelberg, Apr. 2004. doi: 10.1007/978-3-540-39918-6_74.

Calkins, J. A., Offield, T. W., Abdullah, S., and Ali, S. *Geology of the southern Himalaya in Hazara, Pakistan, and adjacent areas*. 1975. doi: 10.3133/pp716c.

Chen, K., Xu, W., Mai, P. M., Gao, H., Zhang, L., and Ding, X. The 2017 Mw 7.3 Sarpol Zahāb Earthquake, Iran: A compact blind shallow-dipping thrust event in the mountain front fault basement. *Tectonophysics*, 747–748:108–114, Nov. 2018. doi: 10.1016/j.tecto.2018.09.015.

Chung, C.-J. F. and Fabbri, A. G. Validation of Spatial Prediction Models for Landslide Hazard Mapping. *Natural Hazards*, 30(3): 451–472, Nov. 2003. doi: 10.1023/b:nhaz.0000007172.62651.2b.

Dafni, J. and Wartman, J. Centrifuge Studies of Topographic Effects: Dynamic Response Mechanisms. *Bulletin of the Seismological Society of America*, 111(4):2101–2111, June 2021. doi: 10.1785/0120200353.

Dahal, A., Tanyaş, H., and Lombardo, L. Full seismic waveform analysis combined with transformer neural networks improves coseismic landslide prediction. *Communications Earth & Environment*, 5(1), Feb. 2024. doi: 10.1038/s43247-024-01243-8.

Dobry, R., Borcherdt, R. D., Crouse, C. B., Idriss, I. M., Joyner, W. B., Martin, G. R., Power, M. S., Rinne, E. E., and Seed, R. B. New Site Coefficients and Site Classification System Used in Recent

Building Seismic Code Provisions. *Earthquake Spectra*, 16(1): 41–67, Feb. 2000. doi: 10.1193/1.1586082.

Dunham, A. Supplementary Movies for "The influence of ground shaking on the distribution and size of coseismic landslides from the Mw 7.6 2005 Kashmir earthquake", July 2024. doi: 10.5281/zenodo.12534705.

Dunham, A. M., Kiser, E., Kargel, J. S., Haritashya, U. K., Watson, C. S., Shugar, D. H., Hughes, A., and DeCelles, P. G. Topographic Control on Ground Motions and Landslides From the 2015 Gorkha Earthquake. *Geophysical Research Letters*, 49(10), May 2022. doi: 10.1029/2022gl098582.

Dunning, S., Mitchell, W., Rosser, N., and Petley, D. The Hattian Bala rock avalanche and associated landslides triggered by the Kashmir Earthquake of 8 October 2005. *Engineering Geology*, 93 (3–4):130–144, Aug. 2007. doi: 10.1016/j.enggeo.2007.07.003.

Fan, X., Domènech, G., Scaringi, G., Huang, R., Xu, Q., Hales, T. C., Dai, L., Yang, Q., and Francis, O. Spatio-temporal evolution of mass wasting after the 2008 Mw 7.9 Wenchuan earthquake revealed by a detailed multi-temporal inventory. *Landslides*, 15 (12):2325–2341, Sept. 2018. doi: 10.1007/s10346-018-1054-5.

Fan, X., Scaringi, G., Korup, O., West, A. J., van Westen, C. J., Tanyas, H., Hovius, N., Hales, T. C., Jibson, R. W., Allstadt, K. E., Zhang, L., Evans, S. G., Xu, C., Li, G., Pei, X., Xu, Q., and Huang, R. Earthquake-Induced Chains of Geologic Hazards: Patterns, Mechanisms, and Impacts. *Reviews of Geophysics*, 57(2): 421–503, June 2019. doi: 10.1029/2018rg000626.

Farr, T. G., Rosen, P. A., Caro, E., Crippen, R., Duren, R., Hensley, S., Kobrick, M., Paller, M., Rodriguez, E., Roth, L., Seal, D., Shaffer, S., Shimada, J., Umland, J., Werner, M., Oskin, M., Burbank, D., and Alsdorf, D. The Shuttle Radar Topography Mission. *Reviews of Geophysics*, 45(2), 2007. doi: https://doi.org/10.1029/2005RG000183.

Gorum, T., Fan, X., van Westen, C. J., Huang, R. Q., Xu, Q., Tang, C., and Wang, G. Distribution pattern of earthquake-induced landslides triggered by the 12 May 2008 Wenchuan earthquake. *Geomorphology*, 133(3–4):152–167, Oct. 2011. doi: 10.1016/j.geomorph.2010.12.030.

Gorum, T., Korup, O., van Westen, C. J., van der Meijde, M., Xu, C., and van der Meer, F. D. Why so few? Landslides triggered by the 2002 Denali earthquake, Alaska. *Quaternary Science Reviews*, 95:80–94, July 2014. doi: 10.1016/j.quascirev.2014.04.032.

Graves, R. and Pitarka, A. Broadband ground-motion simulation using a hybrid approach. *Bulletin of the Seismological Society of America*, 100(5 A):2095–2123. doi: 10.1785/0120100057.

Görüm, T., Tanyas, H., Karabacak, F., Yılmaz, A., Girgin, S., Allstadt, K. E., Süzen, M. L., and Burgi, P. Preliminary documentation of coseismic ground failure triggered by the February 6, 2023 Türkiye earthquake sequence. *Engineering Geology*, 327: 107315, Dec. 2023. doi: 10.1016/j.enggeo.2023.107315.

Hailemikael, S., Lenti, L., Martino, S., Paciello, A., Rossi, D., and Mugnozza, G. S. Ground-motion amplification at the Colle di Roio ridge, central Italy: a combined effect of stratigraphy and topography. *Geophysical Journal International*, 206(1):1–18, Apr. 2016. doi: 10.1093/gji/ggw120.

Harp, E. L. and Crone, A. J. *Landslides triggered by the October 8, 2005, Pakistan earthquake and associated landslide-dammed reservoirs*. 2006. doi: 10.3133/ofr20061052.

Harp, E. L., Hartzell, S. H., Jibson, R. W., Ramirez-Guzman, L., and Schmitt, R. G. Relation of Landslides Triggered by the Kiholo Bay Earthquake to Modeled Ground Motion. *Bulletin of the Seismological Society of America*, 104(5):2529–2540, Sept. 2014. doi: 10.1785/0120140047.

Hartzell, S., Meremonte, M., Ramirez-Guzman, L., and McNamara, D. Ground Motion in the Presence of Complex Topography: Earthquake and Ambient Noise Sources. *Bulletin of the Seismological Society of America*, 104(1):451–466, Nov. 2013. doi: 10.1785/0120130088.

Hartzell, S., Ramírez-Guzmán, L., Meremonte, M., and Leeds, A. Ground Motion in the Presence of Complex Topography II: Earthquake Sources and 3D Simulations. *Bulletin of the Seismological Society of America*, 107(1):344–358, Dec. 2016. doi: 10.1785/0120160159.

Huang, R., Pei, X., Fan, X., Zhang, W., Li, S., and Li, B. The characteristics and failure mechanism of the largest landslide triggered by the Wenchuan earthquake, May 12, 2008, China. *Landslides*, 9(1):131–142, June 2011. doi: 10.1007/s10346-011-0276-6.

Héloïse, C., Bard, P.-Y., and Rodriguez-Marek, A. Site effect assessment using KiK-net data: Part 1. A simple correction procedure for surface/downhole spectral ratios. *Bulletin of Earthquake Engineering*, 10(2):421–448, May 2011. doi: 10.1007/s10518-011-9283-1.

Jibson, R. W. and Tanyaş, H. The influence of frequency and duration of seismic ground motion on the size of triggered landslides—A regional view. *Engineering Geology*, 273:105671, Aug. 2020. doi: 10.1016/j.enggeo.2020.105671.

Jibson, R. W., Harp, E. L., and Michael, J. A. A method for producing digital probabilistic seismic landslide hazard maps. *Engineering Geology*, 58(3–4):271–289, Dec. 2000. doi: 10.1016/s0013-7952(00)00039-9.

Kagawa, T., Irikura, K., and Somerville, P. G. Differences in ground motion and fault rupture process between the surface and buried rupture earthquakes. *Earth, Planets and Space*, 56(1): 3–14, June 2004. doi: 10.1186/bf03352486.

Kamp, U., Growley, B. J., Khattak, G. A., and Owen, L. A. GIS-based landslide susceptibility mapping for the 2005 Kashmir earthquake region. *Geomorphology*, 101(4):631–642, Nov. 2008. doi: 10.1016/j.geomorph.2008.03.003.

Kamp, U., Owen, L. A., Growley, B. J., and Khattak, G. A. Back analysis of landslide susceptibility zonation mapping for the 2005 Kashmir earthquake: an assessment of the reliability of susceptibility zoning maps. *Natural Hazards*, 54(1):1–25, Sept. 2009. doi: 10.1007/s11069-009-9451-7.

Kaneda, H., Nakata, T., Tsutsumi, H., Kondo, H., Sugito, N., Awata, Y., Akhtar, S. S., Majid, A., Khattak, W., Awan, A. A., Yeats, R. S., Hussain, A., Ashraf, M., Wesnousky, S. G., and Kausar, A. B. Surface Rupture of the 2005 Kashmir, Pakistan, Earthquake and Its Active Tectonic Implications. *Bulletin of the Seismological Society of America*, 98(2):521–557, Apr. 2008. doi: 10.1785/0120070073.

Kennett, B. L. N. and Engdahl, E. R. Traveltimes for global earthquake location and phase identification. *Geophysical Journal International*, 105(2):429–465, May 1991. doi: 10.1111/j.1365-246x.1991.tb06724.x.

Khan, S., van der Meijde, M., van der Werff, H., and Shafique, M. The impact of topography on seismic amplification during the 2005 Kashmir earthquake. *Natural Hazards and Earth System Sciences*, 20(2):399–411, Feb. 2020. doi: 10.5194/nhess-20-399-2020.

Khan, S. F., Kamp, U., and Owen, L. A. Documenting five years of landsliding after the 2005 Kashmir earthquake, using repeat photography. *Geomorphology*, 197:45–55, Sept. 2013. doi: 10.1016/j.geomorph.2013.04.033.

Khattak, G. A., Owen, L. A., Kamp, U., and Harp, E. L. Evolution of earthquake-triggered landslides in the Kashmir Himalaya, northern Pakistan. *Geomorphology*, 115(1–2):102–108, Feb. 2010. doi: 10.1016/j.geomorph.2009.09.035.

Komatitsch, D. and Tromp, J. Introduction to the spectral element method for three-dimensional seismic wave propagation. *Geo-*

physical Journal International, 139(3):806–822, Dec. 1999. doi: 10.1046/j.1365-246x.1999.00967.x.

Komatitsch, D. and Tromp, J. Spectral-element simulations of global seismic wave propagation-I. Validation. *Geophysical Journal International*, 149(2):390–412, May 2002a. doi: 10.1046/j.1365-246x.2002.01653.x.

Komatitsch, D. and Tromp, J. Spectral-element simulations of global seismic wave propagation-II. Three-dimensional models, oceans, rotation and self-gravitation. *Geophysical Journal International*, 150(1):303–318, July 2002b. doi: 10.1046/j.1365-246x.2002.01716.x.

Konagai, K. and Sattar, A. Partial breaching of Hattian Bala Landslide Dam formed in the 8th October 2005 Kashmir Earthquake, Pakistan. *Landslides*, 9(1):1–11, July 2011. doi: 10.1007/s10346-011-0280-x.

Konno, K. and Ohmachi, T. Ground-motion characteristics estimated from spectral ratio between horizontal and vertical components of microtremor. *Bulletin of the Seismological Society of America*, 88(1):228–241, Feb. 1998. doi: 10.1785/bssa0880010228.

Kramer, S. *Geotechnical Earthquake Engineering*. Prentice-Hall, 1996.

Lee, S., Chen, H., and Ma, K. Strong ground motion simulation of the 1999 Chi-Chi, Taiwan earthquake from a realistic three-dimensional source and crustal structure. *Journal of Geophysical Research: Solid Earth*, 112(B6), June 2007. doi: 10.1029/2006jb004615.

Lee, S.-J., Chan, Y.-C., Komatitsch, D., Huang, B.-S., and Tromp, J. Effects of Realistic Surface Topography on Seismic Ground Motion in the Yangminshan Region of Taiwan Based Upon the Spectral-Element Method and LiDAR DTM. *Bulletin of the Seismological Society of America*, 99(2A):681–693, Apr. 2009. doi: 10.1785/0120080264.

Mahesh, P., Rai, S. S., Sivaram, K., Paul, A., Gupta, S., Sarma, R., and Gaur, V. K. One-Dimensional Reference Velocity Model and Precise Locations of Earthquake Hypocenters in the Kumaon–Garhwal Himalaya. *Bulletin of the Seismological Society of America*, 103(1):328–339, Feb. 2013. doi: 10.1785/0120110328.

Mahmood, I., Qureshi, S. N., Tariq, S., Atique, L., and Iqbal, M. F. Analysis of Landslides Triggered by October 2005, Kashmir Earthquake. *PLoS Currents*, 2015. doi: 10.1371/currents.dis.0bc3ebc5b8adf5c7fe9fd3d702d44a99.

Marano, K. D., Wald, D. J., and Allen, T. I. Global earthquake casualties due to secondary effects: a quantitative analysis for improving rapid loss analyses. *Natural Hazards*, 52(2):319–328, Apr. 2009. doi: 10.1007/s11069-009-9372-5.

Marc, O., Hovius, N., Meunier, P., Gorum, T., and Uchida, T. A seismologically consistent expression for the total area and volume of earthquake-triggered landsliding. *Journal of Geophysical Research: Earth Surface*, 121(4):640–663, Apr. 2016. doi: 10.1002/2015jf003732.

Marc, O., Stumpf, A., Malet, J.-P., Gosset, M., Uchida, T., and Chiang, S.-H. Initial insights from a global database of rainfall-induced landslide inventories: the weak influence of slope and strong influence of total storm rainfall. *Earth Surface Dynamics*, 6(4): 903–922, Oct. 2018. doi: 10.5194/esurf-6-903-2018.

Massa, M., Barani, S., and Lovati, S. Overview of topographic effects based on experimental observations: meaning, causes and possible interpretations. *Geophysical Journal International*, 197(3):1537–1550, May 2014. doi: 10.1093/gji/ggt341.

Massey, C., Townsend, D., Rathje, E., Allstadt, K. E., Lukovic, B., Kaneko, Y., Bradley, B., Wartman, J., Jibson, R. W., Petley, D. N., Horspool, N., Hamling, I., Carey, J., Cox, S., Davidson, J., Dellow, S., Godt, J. W., Holden, C., Jones, K., Kaiser, A., Little, M., Lyndsell, B., McColl, S., Morgenstern, R., Rengers, F. K., Rhoades, D., Rosser, B., Strong, D., Singeisen, C., and Villeneuve, M. Landslides Triggered by the 14 November 2016 Mw 7.8 Kaikōura Earthquake, New Zealand. *Bulletin of the Seismological Society of America*, 108(3B):1630–1648, Mar. 2018. doi: 10.1785/0120170305.

Maufroy, E., Cruz-Atienza, V. M., Cotton, F., and Gaffet, S. Frequency-Scaled Curvature as a Proxy for Topographic Site-Effect Amplification and Ground-Motion Variability. *Bulletin of the Seismological Society of America*, 105(1):354–367, Dec. 2014. doi: 10.1785/0120140089.

Meunier, P., Hovius, N., and Haines, A. J. Regional patterns of earthquake-triggered landslides and their relation to ground motion. *Geophysical Research Letters*, 34(20), Oct. 2007. doi: 10.1029/2007gl031337.

Meunier, P., Hovius, N., and Haines, J. A. Topographic site effects and the location of earthquake induced landslides. *Earth and Planetary Science Letters*, 275(3–4):221–232, Nov. 2008. doi: 10.1016/j.epsl.2008.07.020.

Mir, R. R., Parvez, I. A., Gaur, V. K., Ashish, Chandra, R., and Romshoo, S. A. Crustal Structure beneath the Kashmir Basin Adjoining the Western Himalayan Syntaxis. *Bulletin of the Seismological Society of America*, 107(5):2443–2458, Sept. 2017. doi: 10.1785/0120150334.

Nowicki Jessee, M. A., Hamburger, M. W., Allstadt, K., Wald, D. J., Robeson, S. M., Tanyas, H., Hearne, M., and Thompson, E. M. A Global Empirical Model for Near-Real-Time Assessment of Seismically Induced Landslides. *Journal of Geophysical Research: Earth Surface*, 123(8):1835–1859, Aug. 2018. doi: 10.1029/2017jf004494.

Oglesby, D. D., Archuleta, R. J., and Nielsen, S. B. Earthquakes on Dipping Faults: The Effects of Broken Symmetry. *Science*, 280(5366):1055–1059, May 1998. doi: 10.1126/science.280.5366.1055.

Owen, L. A., Kamp, U., Khattak, G. A., Harp, E. L., Keefer, D. K., and Bauer, M. A. Landslides triggered by the 8 October 2005 Kashmir earthquake. *Geomorphology*, 94(1–2):1–9, Feb. 2008. doi: 10.1016/j.geomorph.2007.04.007.

Paolucci, R. Amplification of earthquake ground motion by steep topographic irregularities. *Earthquake Engineering & Structural Dynamics*, 31(10):1831–1853, July 2002. doi: 10.1002/eqe.192.

Parsons, T., Yeats, R. S., Yagi, Y., and Hussain, A. Static stress change from the 8 October, 2005 M = 7.6 Kashmir earthquake. *Geophysical Research Letters*, 33(6), Mar. 2006. doi: 10.1029/2005gl025429.

Patera, A. T. A spectral element method for fluid dynamics: Laminar flow in a channel expansion. *Journal of Computational Physics*, 54(3):468–488, June 1984. doi: 10.1016/0021-9991(84)90128-1.

Pathier, E., Fielding, E. J., Wright, T. J., Walker, R., Parsons, B. E., and Hensley, S. Displacement field and slip distribution of the 2005 Kashmir earthquake from SAR imagery. *Geophysical Research Letters*, 33(20), Oct. 2006. doi: 10.1029/2006gl027193.

Peiris, N., Rossetto, T., Burton, P., and Mahmood, S. EEFIT Mission: October 8, 2005 Kashmir Earthquake. In published report,, The Institution of Structural Engineers, 2006.

Petley, D., Dunning, S., Rosser, N., and Kausar, A. Incipient Landslides in the Jhelum Valley, Pakistan Following the 8th October 2005 Earthquake. In *Disaster mitigation of debris flows, slope failures and landslides*, volume 47 of *Frontiers of Science Series*. 2006.

Rault, C., Robert, A., Marc, O., Hovius, N., and Meunier, P. Seismic and geologic controls on spatial clustering of landslides in three large earthquakes. *Earth Surface Dynamics*, 7(3):829–839, Sept. 2019. doi: 10.5194/esurf-7-829-2019.

Rault, C., Chao, W.-A., Gelis, C., Burtin, A., Chang, J.-M., Marc, O., Lai, T.-S., Wu, Y.-M., Hovius, N., and Meunier, P. Seismic Response of a Mountain Ridge Prone to Landsliding. *Bulletin of the Seismological Society of America*, 110(6):3004–3020, July 2020. doi: 10.1785/0120190127.

Saba, S. B., van der Meijde, M., and van der Werff, H. Spatiotemporal landslide detection for the 2005 Kashmir earthquake region. *Geomorphology*, 124(1–2):17–25, Dec. 2010. doi: 10.1016/j.geomorph.2010.07.026.

Sarfraz, Y., Basharat, M., Riaz, M. T., Akram, M. S., Ahmed, K. S., and Shahzad, A. Spatio-temporal evolution of landslides along transportation corridors of Muzaffarabad, Northern Pakistan. *Environmental Earth Sciences*, 82(5), Mar. 2023. doi: 10.1007/s12665-023-10822-5.

Sato, H. P., Hasegawa, H., Fujiwara, S., Tobita, M., Koarai, M., Une, H., and Iwahashi, J. Interpretation of landslide distribution triggered by the 2005 Northern Pakistan earthquake using SPOT 5 imagery. *Landslides*, 4(2):113–122, Dec. 2007. doi: 10.1007/s10346-006-0069-5.

Sattar, A. and Konagai, K. *Post-formation Behavior of Hattian Landslide Dam and Post-breaching Situation*, page 299–309. Springer Nature Switzerland, 2023. doi: 10.1007/978-3-031-44296-4_16.

Shafique, M. Spatial and temporal evolution of co-seismic landslides after the 2005 Kashmir earthquake. *Geomorphology*, 362: 107228, Aug. 2020. doi: 10.1016/j.geomorph.2020.107228.

Shafique, M., van der Meijde, M., and Khan, M. A. A review of the 2005 Kashmir earthquake-induced landslides; from a remote sensing prospective. *Journal of Asian Earth Sciences*, 118:68–80, Mar. 2016. doi: 10.1016/j.jseaes.2016.01.002.

Tanyaş, H., Allstadt, K. E., and van Westen, C. J. An updated method for estimating landslide-event magnitude. *Earth Surface Processes and Landforms*, 43(9):1836–1847, Mar. 2018. doi: 10.1002/esp.4359.

Valagussa, A., Marc, O., Frattini, P., and Crosta, G. Seismic and geological controls on earthquake-induced landslide size. *Earth and Planetary Science Letters*, 506:268–281, Jan. 2019. doi: 10.1016/j.epsl.2018.11.005.

Xu, C., Xu, X., Yao, X., and Dai, F. Three (nearly) complete inventories of landslides triggered by the May 12, 2008 Wenchuan Mw 7.9 earthquake of China and their spatial distribution statistical analysis. *Landslides*, 11(3):441–461. doi: 10.1007/s10346-013-0404-6.

Yan, Y., Pinel, V., Trouvé, E., Pathier, E., Perrin, J., Bascou, P., and Jouanne, F. Coseismic displacement field and slip distribution of the 2005 Kashmir earthquake from SAR amplitude image correlation and differential interferometry. *Geophysical Journal International*, 193(1):29–46, Jan. 2013. doi: 10.1093/gji/ggs102.